Nano Research

ISSN 1998-0124 CN 11-5974/O4
https://doi.org/10.1007/s12274-019-2371-2

Research Article

Post-synthesis phase and shape evolution of $CsPbBr_3$ colloidal nanocrystals: The role of ligands

Elisabetta Fanizza[1,2,§] (✉), Francesca Cascella[1,†,§], Davide Altamura[3], Cinzia Giannini[3], Annamaria Panniello[2], Leonardo Triggiani[1,2], Francesca Panzarea[1], Nicoletta Depalo[2], Roberto Grisorio[4,5], Gianpaolo Suranna[4,5], Angela Agostiano[1,2], M. Lucia Curri[1,2], and Marinella Striccoli[2] (✉)

[1] *Dipartimento di Chimica, Università degli Studi di Bari "A. Moro", Via Orabona 4 , 70126 Bari, Italy*
[2] *CNR-Istituto per i Processi Chimico Fisici, S. S. Bari, Via Orabona, 4, 70126 Bari, Italy*
[3] *CNR-Istituto di Cristallografia, Via Amendola, 122/O, 70126 Bari, Italy*
[4] *Dipartimento di Ingegneria Civile, Ambientale, del Territorio, Edile e di Chimica (DICATECh), Politecnico di Bari, Via Orabona 4, 70125, Italy*
[5] *CNR-NANOTEC- Istituto di Nanotecnologia, Via Monteroni 73100 Lecce, Italy*
[†] *Present Address: Max Planck Institute for Dynamics of Complex Technical Systems, Physical and Chemical Foundations of Process Engineering, Sandtorstr.1, D-39106 Magdeburg, Germany*
[§] *Elisabetta Fanizza and Francesca Cascella contributed equally to this work.*

Received: 15 October 2018 / **Revised:** 25 February 2019 / **Accepted:** 5 March 2019

ABSTRACT

The surface chemistry of colloidal cesium lead bromide ($CsPbBr_3$) nanocrystals is decisive in determining the stability and the final morphology of this class of materials, characterized by ionic structure and a high defect tolerance factor. Here, the high sensitivity of purified colloidal nanocubes of $CsPbBr_3$ to diverse environmental condition (solvent dilution, ageing, ligands post synthetic treatment) in ambient atmosphere is investigated by means of a comprehensive morphological (electron microscopy), structural ($\theta/2\theta$ X-ray diffraction (XRD) and grazing incidence wide angle scattering (GIWAXS)), and spectroscopic chemical (^{1}H nuclear magnetic resonance (NMR), nuclear Overhauser effect spectroscopy (NOESY), absorption and emission spectroscopy) characterization. The aging and solvent dilution contribute to modify the nanocrystal morphology, due to a modification of the ligand dynamic. Moreover, we establish the ability of aliphatic carboxylic acids and alkyl amines ligands to induce, even in a post preparative process at room temperature, structural, morphological and spectroscopic variations. Upon post synthesis alkyl amine addition, in particular of oleyl amine and octyl amine, the highly green emitting $CsPbBr_3$ nanocubes effectively turn into one-dimensional (1D) thin tetragonal nanowires or lead halide deficient rhombohedral zero-dimensional (0D) Cs_4PBBr_6 structures with a complete loss of fluorescence. The addition of an alkyl carboxylic acid, as oleic and nonanoic acid, produces the transformation of nanocubes into still emitting orthorombic two-dimensional (2D) nanoplates. The acid/base equilibrium between the native and added ligands, the adsorbed/free ligands dynamic in solution and the ligand solubility in non-polar solvent contribute to render $CsPbBr_3$ particularly sensitive to environmental and processing conditions and, therefore prone to undergo to structural, morphological and, hence spectroscopic, transformations.

KEYWORDS

lead halide perovskite nanocrystals, surface chemistry, ligands equilibria, long term stability

1 Introduction

Since the first reports on solution phase synthesis [1], all-inorganic cesium lead halide perovskite (CsLHP) nanocrystals (NCs) have shown exceptional photophysical properties, greatly enhanced compared to those of conventional chalcogenides [2–4]. Such excellent optoelectronic properties include a direct band gap tunability over the entire visible spectral range by control of NC size and composition through anion exchange, a large optical absorption cross section, a very bright emission with high photoluminescence (PL) quantum yield (QY), a long carrier diffusion length and a large charge carrier mobility [5]. The outstanding characteristics of CsLHP NCs, accounted by the ionic structure and the high defect tolerance factor [3, 4], are, however, hampered by the stability issues of this class of materials. In fact, the all-inorganic colloidal CsLHP, although less thermal/moisture sensitive than the organic–inorganic counterpart [4, 6], still presents limitations in term of stability, thus requiring care and attention in processing and for their integration in devices [7]. In particular, the ionic nature of CsLHP NCs is responsible of their fast deterioration that may result in NC dissolution in solution, further accelerated by their high surface area. As an example, purification procedures and redispersion in solvent of the as synthesized colloidal CsLHP NCs have been reported as crucial steps, able to induce NC destabilization. Solvents as acetone [1], tert-butyl alcohol [1], ethyl acetate [8], and isopropyl alcohol [9] with a relatively low polarity [10] are used as non-solvents in purification procedures, rather than the generally used protic solvents as methanol and ethanol, presenting a polarity too high to preserve the CsLHP integrity. Accordingly, solvents like anhydrous hexane or toluene, with polarity lower than chloroform, are used to disperse the CsLHP NCs. A key role in the limited stability of the CsLHP NCs has been also accounted to the

Address correspondence to Elisabetta Fanizza, elisabetta.fanizza@uniba.it; Marinella Striccoli, m.striccoli@ba.ipcf.cnr.it

organic–inorganic interaction between alkyl amine and alkyl carboxylic acid, used as ligands, and the NC surface [11–13]. Irrespectively of the synthetic protocol, that may be based on solution phase hot injection [1, 8, 12, 14–21] or ligand assisted precipitation at room temperature [22–26], alkyl amine and carboxylic acid have shown their potential in regulating the final morphology of the NCs, promoting the selective formation of nanocubes [1, 12, 14], nanoplates (NPLs) [16–18, 21], nanowires (NWs) [8, 20], acting on an acid base equilibrium mechanism [18]. Moreover, alkyl amine and carboxylic acid have been proven essential to determine the surface chemistry of the nanostructures [11, 12]. Indeed, alkyl amine (mainly oleylamine, Olam) or carboxylic acid (mainly oleic acid, Olac) are reported to behave as Lewis base and acid, respectively, stabilizing the NCs in solution with alkylammonium, forming hydrogen bond with bromide anionic surface sites, and alkyl carboxylate binding the surface cationic sites. However, ligands interaction [11] with the NC surface is labile and causes rapid desorption of the protective ligand layer, for example upon isolation and purification of colloids, affecting the colloidal stability and optical properties [12, 13, 27]. Recently, Krieg F. et al. [27] described the improved chemical stability and preserved PL properties of CsLHP NCs prepared by hot injection procedures by replacing alkyl amines and carboxylic acids with zwitterionic ligands, able to coordinate simultaneously the surface cations and anions, thus pointing out the essential role of surface chemistry in CsLHP NC stabilization. However, the use of these bifunctional zwitterionic ligands poses strong limitation to the ability of effectively engineering the morphology of the final nanostructures through the versatile combinations of both alkyl amine and carboxylic acid as ligands.

The dynamic binding of the ligands to the NC surface, the acid-base equilibrium between organic acid and base ligands, the low energy formation, which makes the surfactant controlled recrystallization of free ions in solution a viable process at room temperature, all contribute to render CsLHP materials particularly sensitive to environmental and processing conditions and prone to undergo to structural, morphological and, hence spectroscopic, transformations.

In this perspective, here, we investigate the effect of post-preparative treatments on $CsPbBr_3$ colloidal nanocubes, prepared by hot injection approach. Among the all-inorganic CsLHP, numerous studies focus on $CsPbBr_3$, more stable in terms of photophysical properties under ambient condition than $CsPbI_3$. In fact, iodide based NCs obtained in the cubic phase at high temperature turn into the photoinactive orthorhombic δ-$CsPbI_3$ phase below 100 °C [28]. Nonetheless, a versatile and reversible conversion of three-dimensional (3D) $CsPbBr_3$ nanocubes to zero-dimensional (0D) rhombohedral lead halide deficient non perovskite Cs_4PbBr_6 nanostructures by post-synthetic temperature and chemical treatments with alkyl amine has been recently reported [29–34], pointing out the softness of $CsPbBr_3$ [35, 36].

Here, we report on the systematic investigation of the spectroscopic, morphological, structural and surface chemistry properties evolution of as prepared $CsPbBr_3$ nanocubes upon ligand addition (alkyl carboxylic acid or alkyl amine mainly oleic and nonanoic acid (NA), and oleil and octylamine (OCTA), respectively), solvent dilution and ageing experiments. In particular, the post-synthetic treatment with alkyl carboxylic acid or alkyl amine induces a surfactant controlled transformation of 3D nanocubes into two-dimensional (2D) NPLs, when Olac is added, and into one-dimensional (1D) NWs and 0D Cs_4PbBr_6 crystals, respectively, when Olam is adjoined at room temperature. Interestingly, the observed deterioration of $CsPBr_3$ colloidal NCs is mainly ascribed to modification of ligand equilibria, also driven by the ionic structure of CsLHP and low energy formation, finally resulting in severe structural and morphological transformations and, consequently, changes in the optoelectronic properties.

2 Experimental section

2.1 Materials

$PbBr_2$ (98%), octadecene (ODE, 90%), oleic acid (Olac, 90%), oleylamine (Olam, 70%), octylamine (OCTA, 99%), nonanoic acid (NA, 96%), Cs_2CO_3 (99.9%), %), hexane (anhydrous 95%) and benzene-d_6 were purchased from Sigma-Aldrich and used without any further purification.

2.1.1 *Solution-based synthesis of colloidal $CsPbBr_3$ NCs*

The synthesis of $CsPbBr_3$ NCs was carried out according to the procedure reported by Protesescu et al. with minor modifications [1]. A mixture of 0.4 mmol of $PbBr_2$, 10 mL of ODE (40 mM), 3.0 mmol of Olac (0.3 M) and 3.0 mmol of fresh Olam (0.3 M) was prepared in a three necked flask and put under vacuum at 80 °C for 1 h and at 150 °C under nitrogen flux for 30 min. In a second three-necked flask the cesium precursor was prepared by dispersing 0.4 mmol of Cs_2CO_3 in 5mL of ODE ($[Cs^+]$ = 80 mM) with 2.5 mmol of Olac (0.5 mM). The mixture, firstly put under vacuum at 100 °C for 1 h, was subsequently heated to 150 °C under N_2 atmosphere to allow the complete decomposition of Cs_2CO_3 and formation of Cs-oleate (pale yellow solution). 0.8 mL of Cs-Oleate (0.06 mmol) was injected in the lead and bromine mixture at 140 °C suddenly cooled down at room temperature by immersion in ice bath. At this stage, the reaction mixture turns into an intense yellow-green color. The NCs were collected by centrifugation at 9,000 rpm for 90 min at 10 °C without addition of any non-solvent and redispersed in 6 mL of anhydrous hexane. The concentration of this solution is calculated by using the numerical expression of the molar extinction coefficient ε ($\varepsilon = 2 \times 10^{-2}\, d^3$, with d NC average lateral size) reported by J. Maes et al. [37].

Post-synthetic ligand treatments were carried out by adding to 1 mL of the as synthesized $CsPbBr_3$ colloidal solution Olac ranging from 25 μL/mL (0.075 mmol/mL, NC sample named Olac 75) to 50 μL/mL (0.15 mmol/mL, NC sample named Olac 150) or Olam, ranging from 25 μL/mL (0.075 mmol/mL, NC sample named Olam 75) to 50 μL/mL (0.15 mmol/mL, NC sample named Olam 150). The same ligand concentration was used for post synthesis treatment with OCTA and NA, used also in mixture at different molar ratios (OCTA:NA 0.2:1; 0.5:1; 1:1). The samples were then centrifuged at 1,000 rpm for 10 minutes at room temperature and the supernatant recovered for further characterization. Measurements of NC solution pH were carried out by means of litmus paper.

2.2 Characterization techniques

For transmission electron microscopy (TEM) analysis, samples were prepared by dipping a carbon-coated copper grid into the NC solution at 1:100 dilution with anhydrous hexane. TEM imaging was carried out using a JEOL JEM1011 microscope, operating at an accelerating voltage of 100 kV and equipped with a W electron source anda CCD high resolution camera. Statistical analysis of the size (NC average size and size distribution) of the samples was performed by using of Axio Vision software, a freeware image analysis program. The percentage relative standard deviation (σ%) was calculated for each sample, providing information on the NP size distribution. Its value is based on the distribution of size compared to the average value and is expressed as a percentage.

SEM analyses were carried out by means of field emission scanning electron microscopy (FE-SEM) Zeiss Sigma operating in the range 0.5–20 kV and equipped with an in lens secondary electron detector. FE-SEM samples were prepared by spin coating the NC solution at 1,000 and 2,000 rpm for 30 s, with a subsequent

thermal treatment at 40 °C for 5 minutes, to let the solvent to completely evaporate and the spin coated film to dry. The substrates were then placed onto stainless-steel sample holders for SEM measurements.

Ultraviolet–visible (UV–Vis) absorption spectra were recorded with a Cary 5000 (Varian) UV/Vis/NIR spectrophotometer by solvent diluting the NC colloidal solution 1:80.

Fluorescence measurements were performed at room temperature in solution at 1:600 dilution and on solid film by spin coating 50 μL of NC solution onto a quartz 1 cm × 1 cm slide (800 rpm for 30 s), then thermally treated at 40 °C for 5 minutes. Fluorescence spectra were recorded by using a Fluorolog 3 spectrofluorimeter (HORIBA Jobin-Yvon), equipped with double grating excitation and emission monochromators. Time resolved photoluminescence (TRPL) measurements were performed by Time-Correlated Single Photon Counting (TCSPC) technique, with a FluoroHub (HORIBA Jobin-Yvon). The samples were excited at 375 nm by means of a picosecond laser diode (NanoLED 375L) with a pulse length of 80 ps at a 1 MHz repetition rate. The PL signals were dispersed by a double grating monochromator and detected by a picosecond photon counter (TBX ps Photon Detection Module, HORIBA Jobin-Yvon). The temporal resolution of the experimental set up was ~ 200 ps. The values of the absolute quantum yield and 1931 CIE colour point measurements were obtained by means of a "Quanta-phi" integrating sphere coated with Spectralons® and mounted in the optical path of the spectrofluorometer, using as an excitation source a 450 W xenon lamp coupled with a double-grating monochromator.

Grazing incidence wide angle scattering (GIWAXS) patterns were collected at 2° incidence angle with a Rigaku Fr-E+ rotating anode microsource (CuKα radiation) coupled to a SAXS/WAXS camera [37]. An image plate with 100 μm pixel size was used as a detector, placed at 87 mm distance from the sample. Patterns were calibrated by using Ag Behenate standard powder as a reference. Coupled sample-detector X-ray diffraction ($\theta/2\theta$ XRD) scans were collected by a Bruker D8 Discover (CuKα radiation), equipped with a Göbel mirror on the primary beam and a scintillation point detector. Samples for analysis were prepared by drop casting the colloidal solutions on silicon substrates and let evaporate in open air.

For nuclear magnetic resonance (NMR) analysis, the as prepared sample before and after Olam and Olac addition were prepared as follows: 3 mL of the reaction mixture of $CsPbBr_3$ NCs were centrifuged without addition of non-solvent, and the collected precipitate was dried under vacuum for two hours and finally dispersed in C_6D_6. The colloidal solutions (1 mL) of $CsPbBr_3$ NCs treated with Olac and Olam (Olac 75 and Olam 75 and 150) were concentrated by evaporating part of the solvent under nitrogen flux and finally centrifuged, collecting the precipitate for NMR analysis. This procedure allowed to remove free ligand in excess from the solution and to collect the NC for chemical characterization. All the samples were dried under vacuum and dispersed in C_6D_6. ^{1}H-NMR spectra of each samples were recorded at 298.2 K on a Varian 500 MHz spectrometer. The nuclear Overhauser effect spectroscopy (NOESY) was acquired using standard pulse sequences with a mixing time set to 300 ms.

3 Results

3.1 Synthesis and characterization of $CsPbBr_3$ nanocubes

$CsPbBr_3$ NCs are synthesized by using the hot injection approach reported by Protesescu et al. [1]: Cs-oleate precursor (0.06 mmol) is injected at 140 °C in an octadecene solution containing $PbBr_2$ (0.4 mmol), previously dissolved in the presence of an equimolar combination of Olac/Olam (0.3 M/0.3M). TEM characterization of the samples (Fig. 1(a), 1:100 sample dilution), recovered from the reaction mixture by centrifugation and without addition of a non-solvent, shows the presence of square-shaped structures, quite homogenous in size, with a lateral size of 8 nm and size distribution $\sigma\%$ = 17% (Fig. 1(b)). Smaller nanocubes, nearly 4 nm in edge length, are collected at higher centrifugation rate from the supernatant (Fig. S1(e) in the Electronic Supplementary Material (ESM)).

The poor solubility of lead halide precursor in octadecene [14] can be effectively improved by the combined use of both Olam and Olac in the reaction mixture. The binary mixture of alkyl amine and alkyl carboxylic acid ligands does not only serve for precursor solvation, cation coordination and ligand stabilization of the nanostructures, but, according to recent findings, it is involved in the acid-base equilibrium and formation of $Olac^-Olam^+$ [14]. The concentration of ligands and their molar ratio result decisive, along with the control of temperature, for the final CsLHP nanostructure size, shape and phase.

Notably, 140 °C is usually reported [14, 38] as a threshold temperature between the high yield formation of nanocubes (T > 140 °C) and of NPLs (T < 140 °C). However, the equimolar (0.3 M/0.3 M) concentration of Olam and Olac [14] used here in the synthesis (Fig. 1(a)) results mainly in nanocubes with a negligible fraction of NPLs. The UV–Vis absorption spectrum of the as prepared sample (diluted

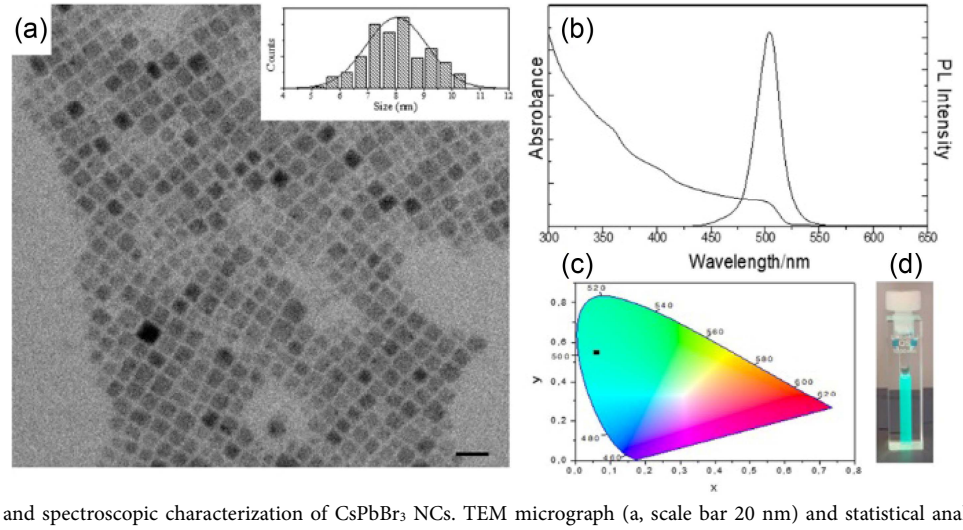

Figure 1 Morphological and spectroscopic characterization of $CsPbBr_3$ NCs. TEM micrograph (a, scale bar 20 nm) and statistical analysis of the NC size (inset, number of counted NCs = 250). UV-Vis absorption spectrum in solution (1:80 sample dilution, 0.12 a.u. absorbance intensity at the first exciton transition) and fluorescence (λex = 375nm) spectrum of NC thin film on quartz prepared by spin coating the NC solution (b) along with the position in the CIE 1931 diagram colour point x = 0.06 y = 0.55 (c). Picture of NC colloidal solution cuvette under illumination with a UV lamp at 365 nm (d).

1:80 with anhydrous hexane, Fig. 1(b)) shows the typical profile of colloidal $CsPbBr_3$ semiconductor nanocubes, characterized by a broad exciton absorption peak at nearly 500 nm [1]. The TEM characterization and the absorption spectrum allow the determination of the molar extinction coefficient, resulting in $\varepsilon = 10\ \mu M^{-1}\cdot cm^{-1}$ for the nanocubes with average lateral size of 8 nm, and a final NC concentration in solution of nearly 10^{-3} M. The PL characterization of the NC samples is purposely carried out in thin film since, upon dilution, a marked transformation of the as prepared nanocubes is observed [39]. Indeed, in order to limit self-absorption phenomena for PL measurements in solution, the NC solutions are diluted up to nearly 10^{-6} M (sample dilution 1:600). At such a concentration, the as synthesized 8 nm sized $CsPbBr_3$ NCs turn into very small nanocubes (Fig. 2(a)), with edge length reduced down to 3 nm, and anisotropic 2D NPLs structures, thus in nano-objects not comparable with what observed before dilution. The PL spectrum of $CsPbBr_3$ NC thin film, prepared by spin coating the colloidal solution on a quartz slide, shows a narrow and intense emission band (full width at half maximum FWHM of 130 meV) centered at 505 nm (2.45 eV). The emission band is associated to the bulk band gap recombination of $CsPbBr_3$ [39] with a value of the absolute QY value of nearly 75%. The coexistence of small NCs and NPLs shown by TEM is also supported by PL characterization (Fig. 2(c), red line). The emission spectrum shows a main band blue shifted to 483 nm (2.57 eV) with a FWHM (150 meV), ascribed to NPLs with a broad distribution in thickness and lateral size, and an additional weak PL contribution at higher energy (2.9 eV) attributed to small NCs. In the meanwhile, the emission dramatically decreases and the PLQY drops down to 30% after dilution, probably due to non-radiative recombination pathways in very small nanostructures and also to the reduced number of emitting nanostructures contributing to the PL [40].

In addition to the dramatic size and shape evolution induced in as prepared $CsPbBr_3$ nanocubes upon dilution, also ageing brings morphological transformation of the nanocubes. Under prolonged (longer than one month) air/moisture and light exposure, the formation of polydispersed larger nanostructures is observed by TEM (Fig. 2(b)), highlighting a limited stability in time of the original nanocubes even on solid phase. This change in morphology is reflected in the PL spectrum, recorded in thin film of NC solution exposed to air. The spectrum presents two contributions (Fig. 2(c), green line) that can be safely assigned on the basis of the TEM characterization (Fig. 2(b)). Namely, the band centered at 505 nm can be ascribed to residual 8 nm-sized nanocubes and the band centered at 519 nm can be attributed to the larger nanostructures, either nanocubes or NPLs with lateral size and thickness up to tens of nanometer. Upon ageing, a progressive PL quenching occurs with a decrease of the PLQY down to 52% after a month.

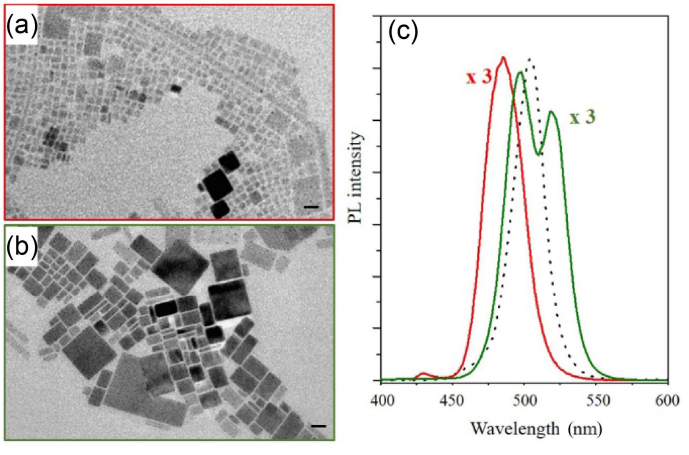

Figure 2 ((a), (b)) TEM micrographs (scale bar 20 nm) and (c) PL spectra (excitation wavelength at 375 nm) of colloidal $CsPbBr_3$ nanocubes just after dilution with hexane at 10^{-6} M concentration ((a) panel, and red line in (c)) and after ageing the dispersion for a month ((b) and green line in (c)). PL spectrum of spin coated as synthesized undiluted colloidal nanocubes solution on quartz slide ((c), dashed line).

3.2 Room temperature ligand induced transformation from 3D nanocubes to 2D nanostructures: morphologic and spectroscopic characterization

3D $CsPbBr_3$ nanocubes transform their structure and spectroscopic properties upon treatment with Olam in solution [14, 29–34]. Several groups [14, 29–34, 41] have claimed the transition of 3D $CsPbBr_3$ nanocubes into 0D Cs_4PbBr_6 rhombohedral nanostructures that crystallize as white powders, upon treatment with Olam in solution. The experiments highlight that the concentration of the oleyl amine, Olam, (although also OCTA has been also tested, Fig. S3 in the ESM) is critical for directing the final morphology, structure and, hence, spectroscopic properties.

In particular, post synthetic addition of 0.075 mmol/mL of Olam to the solution (NC sample named "Olam 75") induces the transformation of the freshly prepared 3D nanocubes into nanostructures similar to nanowires (NWs) over few micrometers long (Figs. 3(a)–3(c)) and 5 nm width (σ% = 18%) along with a small residual fraction of nanocubes.

Such NWs, to the best of our knowledge, have not been isolated, so far, by using such a post-synthetic colloidal approach. Notably, after addition of 0.10 mmol/mL of Olam (Figs. 3(d)–3(f), NC sample named "Olam 100"), the 3D nanocubes turn into NWs tens of nanometers long with nearly 5 nm width together with abundant large spherical nanoparticles of nearly 17 nm in diameter, quite homogenous in size (σ% = 12%). Further, addition of Olam at a concentration > 0.15 M (Figs. 3(g)–3(i), NC sample named "Olam 150") brings to the formation of rhombohedral shaped nanostructures with a lateral size of nearly 18 nm (σ% = 17%) and the separation of a white precipitate.

However, the NWs in Olam 75 sample, although retaining their size and shape regime for more than a weak, slowly turn into larger rhombohedral structures, similar to those reported in Figs. 3(g)–3(i),

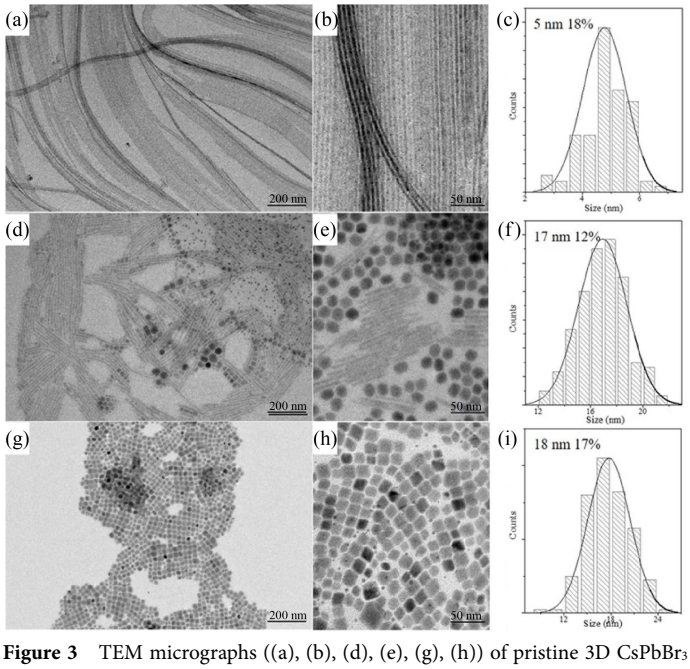

Figure 3 TEM micrographs ((a), (b), (d), (e), (g), (h)) of pristine 3D $CsPbBr_3$ upon addition of ((a) and (b)) 0.075mmol/mL, ((d) and (e)) 0.10 mmol/mL, ((g) and (h)) 0.15 mmol/mL of fresh oleyl amine, resulting in Olam 75, Olam 100 and Olam 150 sample, respectively. Size distribution of the nanowire width (c) in Olam 75, of spherical nanoparticles diameter in Olam 100 (f) and of lateral size of rhombohedral shaped nanostructures in Olam 150 (i) samples.

in approximately three weeks (Figs. S2(a) and S2(c) in the ESM), thus allowing to infer that these nanostructures represent a sort of metastable intermediate.

Similar findings are achieved by adding shorter alkyl chain amine such as OCTA (Fig. S3 in the ESM): The sample shows very thin NWs upon addition of 0.08 M of OCTA and rhombohedral structures at increased OCTA concentration (0.2 M). While the absorption spectrum (Figure 5a orange line) of Olam 75 sample does not show any appreciable changes in exciton position compared to the as synthesized nanocubes (Fig. 5(a), black line), PL spectrum results much more sensitive to the shape transformation with a significant band broadening and a marked quenching, (Fig. 5(b), orange line) with respect to that of the as prepared nanocubes (Fig. 5(b), black line).

The poorly intense emission band centered at 505 nm can be ascribed to the very few residual nanocubes, still detected in the sample by the TEM analysis, while the prominent shoulder at higher energy can be originated by smaller nanostructures (the thin NW), that contribute to the PL at lower wavelength, due to quantum confinement. Meanwhile, the absolute PLQY decreases down to 4%. Since the sample is mainly formed of very thin NWs and only a low amount of residual nanocubes, trap states in thinnest NWs can be involved in non radiative excited electron decay path [42], reducing the PLQY. Additional increase of the Olam amount (Olam 150 sample) results in a completely loss of fluorescence and in a dramatic change of the absorbance spectrum (Fig. 5(a), wine line). The characteristic exciton absorption of the $CsPbBr_3$ turns into a weak signal blue shifted at 430 nm, due to the presence of degraded residual $CsPbBr_3$ very small nanocubes [16], with an intense band at 311 nm, ascribed to the individual $PbBr_6^{4-}$ clusters [14, 32] of the 0D Cs_4PbBr_6, forming at this Olam concentration, as demonstrated by structural investigation (see following section).

While alkyl amine addition promotes the transformation of nanocubes into 1D and rhombohedral nanostructures, well assigned in literature to 0D lead halide depleted nanoparticles, addition of Olac (NA are also tested, Fig. S4(a) in the ESM) to the solution of the as prepared 3D $CsPbBr_3$ nanocubes (Fig. 1(a)) results in the formation of 2D anisotropic nanoplates (Fig. (4)), irrespectively from the amount of Olac added. In particular, with 0.075 mmol/mL of Olac, the pristine nanostructures evolve into 4 nm thick NPLs with a lateral size up to nearly 40 nm (NC sampled named "Olac 75"), sitting with the edge on the TEM grid (Figs. 4(a) and 4(b)) in a typical close packed face-to-face organization [38], although residual 8 nm sized nanocubes can be still observed by TEM characterization.

At higher concentration of Olac (0.15 mmol/mL, NC sample named "Olac 150"), larger platelets are obtained, with lateral size of few hundreds of nanometers (Figs. 4(c) and 4(d)), which preferentially assemble face on the TEM grid. Upon ageing, the small NPLs, that remain stable for more than one week, turn into widely polydisperse NPLs with micrometer sized edge (see Figs. S2(b) and S2(d) in the ESM).

Absorption spectrum of Olac 75 sample (Fig. 5, cyan line) shows an exciton transition signal blue shifted to 485 nm, narrower and

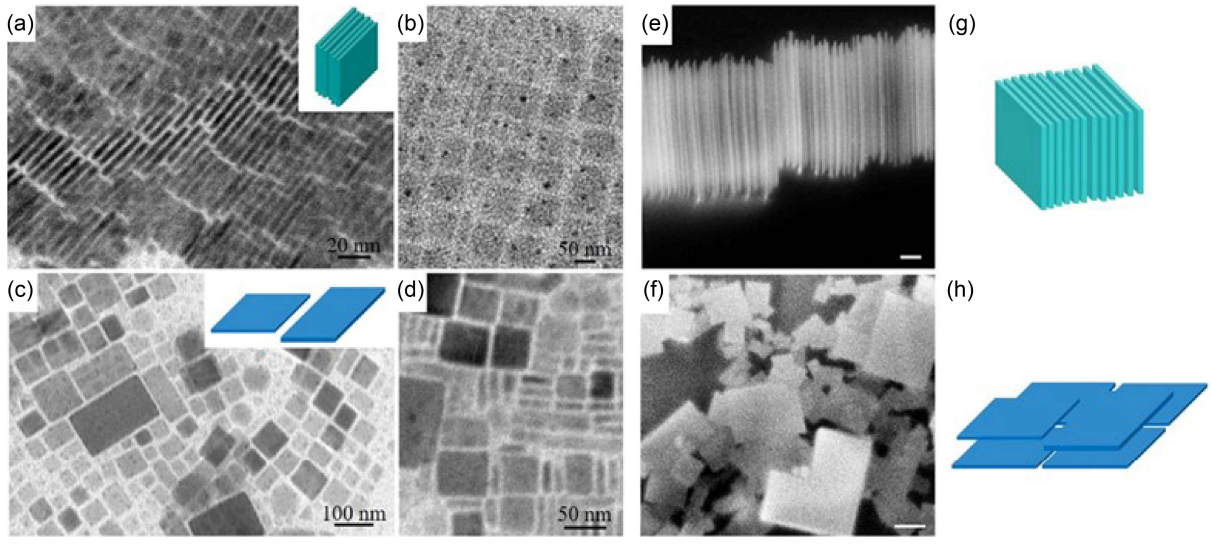

Figure 4 TEM micrographs ((a)–(d)) and SEM images ((e), (f)) of oleic acid (Olac) treated $CsPbBr_3$ nanocubes transforming into nanoplates. TEM images of samples upon addition of 0.075mmol/mL ((a), (b), Olac 75) and 0.15 mmol/mL ((c), (d), Olac 150) of Olac to the as prepared $CsPbBr_3$ nanocubes (see Fig. 1(a)). SEM images ((e), (f), scale bar 100 nm) and schematic sketches ((g), (h)) of stacked ((e), (g)) and lateral-oriented attached ((f), (h)) nanoplates prepared at 0.15 mmol/mL Olac-treatment. Using a spin coating deposition at low speed (1,000 rpm (e)) nanoplates arrange by edge on the substrate facing each other in stacked structures with a long range order, while at high spin speed (2,000 rpm, (f)), nanoplates preferentially lie face on the substrate.

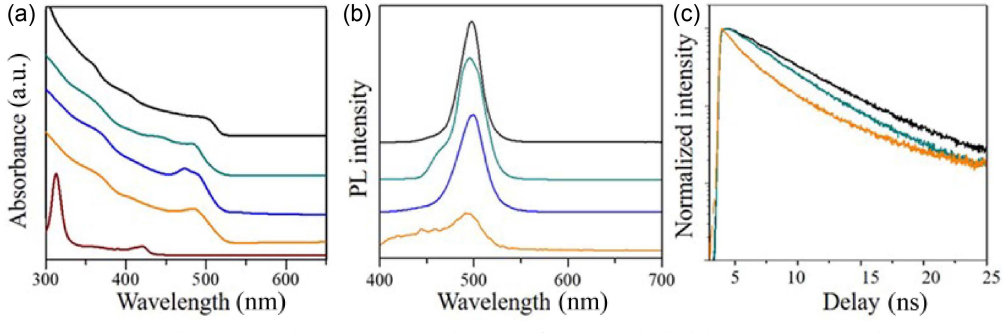

Figure 5 UV–Vis absorbance (a), emission (b) spectra and time resolved PL decay (c) of as prepared (black line), oleyl amine (Olam 75, orange line, Olam 150 wine line) and oleic acid (Olac 75 cyan line and Olac 150 blue line) treated $CsPbBr_3$ samples. The traces are vertically shifted for sake of clarity.

more pronounced with respect to that of the as prepared 3D nanocubes (500 nm), attributed to NPL structures (Fig. 5(a) cyan line) [17, 18, 21, 43–45]. Remarkably, the thickness of the NPLs of 4 nm, approximately corresponding to a three perovskite multilayered structure, is expected to be still in quantum confinement regime [45]. The emission spectrum (Fig. 5(b) cyan line) is characterized by a main band at 503 nm, ascribable to residual nanocubes, and a blue shifted shoulder at nearly 480 nm attributed to NPLs, with thickness smaller than the Bohr diameter [18].

Spectra of Olac 150 sample, obtained upon addition of 0.15 mmol/mL of Olac, shows an exciton absorption signal (Fig. 5(a) blue line) and PL band (Fig. 5(b) blue line), centered at 495 and 505 nm, respectively, consistent with the evolution towards larger NPLs, as confirmed by the TEM characterization. The formation of NPLs turns in an only partial quenching of the emission QY (PLQY 56%) with respect to the as prepared sample.

Time-correlated single photon counting (TCSPC) measurements (Fig. 5(c)) of the as synthesized nanocubes (Fig. 5(c) black line), Olam 75 (Fig. 5(c), orange line) and Olac 75 samples (Fig. 5(c), cyan line), consisting of NWs and NPLs, respectively, deposited in thin films, result well fitted by a three exponential function and the average lifetimes, reported in Table S1 in the ESM, are in line with previous findings [16, 23, 45]. However, a significant difference in the decays of the different nanostructures is evident, even better highlighted on a double logarithmic scale (Fig. S7 in the ESM) in the first few nanoseconds after the excitation. Indeed, the decay of both nanocubes and NPLs shows a faint rise time, not evinced for NWs. This can be ascribed to the large distribution in size of both nanocubes and NPLs, that induces a mechanism of energy transfer among NCs, more pronounced in the samples deposited as thin film, where the nanostructures result in close proximity [46]. The emission from nano-objects of smaller size, properly excited at high energy, can be absorbed rapidly by larger nanostructures, resulting in an increase in the excited population with a delay that originates the rise time phenomenon. In the case of NWs such an effect is not observed, due to the strong PL quenching and the different packing arrangement.

3.3 Room temperature ligand induced transformation from 3D nanocubes to 1D and 2D nanostructures: structural characterization

The results of the systematic structural investigation of the as prepared, aged and post-synthesis treated (with Olam or Olac, at different concentration) samples is reported in Figs. 6 and 7 (see Figs. S5 and S6 in the ESM). It is worth to note that the XRD patterns of each sample have been recorded from films drop cast on silicon substrate, each XRD profile resulting from all the nanostructures composing the sample. The XRD pattern of the as prepared sample, reported in Fig. 6(c) (solid line), well fitted (black line in Fig. S5 in the ESM) using a cubic structure model, confirms the perovskite lattice structure with $CsPbBr_3$ stoichiometry, with a 5.871 Å unit cell size. The 8 nm NC size calculated along the [100] direction is in agreement with the average lateral size of the nanocubes resulting from TEM characterization. However, the significant signal broadening, due to nanocube small size, does not allow to univocally correlate the experimental diffractogram to a specific crystalline phase. Peak positions, indeed, fit with cubic lattice (ICDD #01-072-7930, Fig. 6(a)), monocline (ICDD 00-018-0364, Fig. 6(b)), tetragonal (ICDD #01-074-6645 Fig. 6(g)) and orthorhombic (ICDD #01-072-7929, Fig. 6(h) reference patterns.

It is worth noting that the orthorhombic symmetry should be expected as the thermodynamically stable phase at room temperature for $CsPbBr_3$ crystals, based on literature studies (e.g. [47]) performed on bulk crystals and relatively large nanocrystals (of order 10 nm). However, the very small size, at least on one dimension, of the

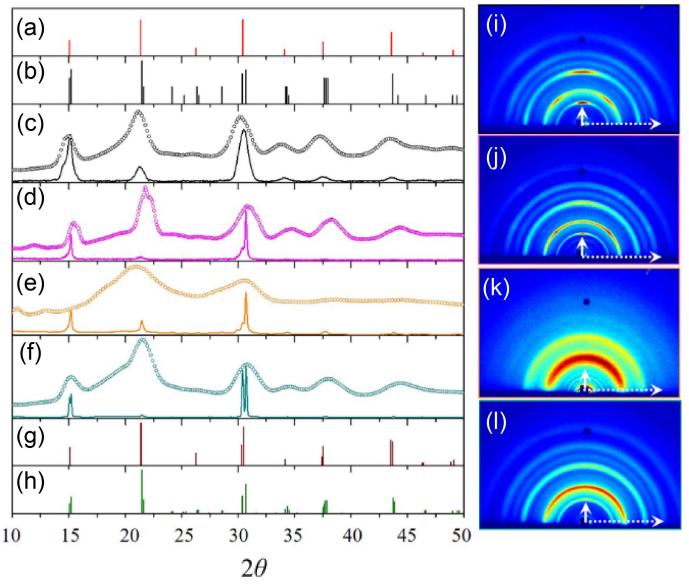

Figure 6 XRD patterns collected in coupled sample-detector ($\theta/2\theta$) scan mode ((c)–(f), solid line), and in grazing incidence (GIWAXS) geometry with 2 degree incidence angle: radial profile ((c)–(f), circle symbol) and 2D maps (i)–(l) of as prepared (c) and (i), one month aged (d) and (j), 0.075 mmol/mL oleyl amine, ((e) and (k), Olam 75) and 0.075 mmol/mL oleic acid ((f), l Olac 75) treated samples. Reference XRD patterns for cubic (ICDD # 01-072-7930, (a)), monoclinic (ICDD 00-018-0364, (b)), tetragonal (ICDD #01-074-6645, (g)) and orthorhombic (ICDD #01-072-7929, (h)).

nanostructures here described, their high shape anisotropy, and susceptibility to environmental-induced transformation (as revealed by morphological and spectroscopic characterization) can leave some ambiguity in defining the actual crystallographic phase, due to both instrumental (peak broadening/overlap) and intrinsic structural (size/strain, unit cell distortions, preferred orientation of NCs) features. Therefore, in the following all the most probable crystal structures for the NCs, based on the available datasheets and literature precedence, are discussed without any assumption.

Here we exploit a combined evaluation of $\theta/2\theta$ XRD patterns and GIWAXS radial profiles, either azimuthally averaged or taken along specific directions (typically in and out of the sample plane, see Fig. S6 in the ESM). $\theta/2\theta$ XRD geometry provides indeed a higher accuracy in terms of peak position and lower instrumental broadening, though the relative intensity of reflections can be affected by NC preferred orientation, possibly resulting in the damping of some reflections compared to reference powder diffraction patterns. On the other hand, the collection of GIWAXS data on a 2D detector allows to readily recognize the presence of preferred orientations; moreover, the profile obtained by fully integrating the scattering intensity along the azimuth is much less affected by preferred orientations, and thus can be directly compared to the diffraction pattern expected for a polycrystalline powder. Therefore, despite the scarcity of details (weak, broad and missing peaks) in the diffraction patterns due to the aforesaid issues, the combined evaluation of the relative main peak intensities, in particular the 2θ = 30.5°/15.1° intensity ratio from the $\theta/2\theta$ XRD profile, and the 30.5°/21.3° ratio from the azimuthally averaged GIWAXS profile, turned out to be helpful in discriminating among different crystalline structures, corresponding to the same perovskite ABX_3 stoichiometry, possibly taken on by the sample in its evolution.

For the cubic phase, the 2θ = 30.5°/15.1° peaks correspond indeed to the $h00$ reflections (i.e. both peaks come from the same lattice planes), which are therefore expected to conserve the ratio of their (integrated) intensities, no matter being affected by NC size/strain broadening and/or preferred orientation. Similarly, in the case of the orthorhombic unit cell, such peaks represent the

convoluted (due to the crystal size and/or instrumental resolution function) intensity of the 00*l*/*hh*0 reflections, which again must overall conserve the ratio between different diffraction orders. A similar argument holds for the monoclinic unit cell, where the two peaks are indexed as 00*l*/*h*00. In any case, peak merging is not an issue in this kind of evaluation, as the integrated intensities of the two diffraction orders will be similarly affected, either by size/strain broadening or by preferred orientations, so that their relative intensity will still be conserved and comparable to that reported for a powder sample. On the contrary, the same argument does not apply for example to the tetragonal phase, where such peaks correspond only partially to different diffraction orders, that is *h*00 and 00*l*/*h*00, respectively (so that the second peak is a convolution of the 002 and 200 reflections): As a consequence, size/strain broadening as well as preferred orientations may differently affect the integrated peak intensities, preventing their overall ratio to be strictly conserved. As explained in the following, the tetragonal phase could be easily ruled out for the early stages of NC evolution, and reconsidered for the nanowires, based on this argument.

In the case of the as prepared sample, the 30.5°/15.1° intensity ratio of nearly 1.1 (Fig. 6(c), solid line) is more characteristic of the monocline (30.5°/15.1° nearly 1, ICDD 00-018-0364) and cubic (30.5°/15.1° nearly 1.3, JCPDS #18-0464) phases rather than matching the orthorhombic (30.5°/15.1° nearly 1.8, ICDD #01-072-7929) one. These values are also smaller than those expected for the tetragonal phase (30.5°/15.1° intensity ratio nearly 3.3, ICDD #01-074-6645) for which the peaks at 15.1° and 30.5° correspond to the 100 and 002/200 reflections, respectively.

The 30.5°/21.3° intensity ratio could only be evaluated from the azimuthally averaged GIWAXS profile, since preferred orientation of the NCs, which is evident from the GIWAXS 2D map in Fig. 5(i), produces a clear damping of the 21.3° peak in the $\theta/2\theta$ XRD pattern, compared to the reference pattern. However, cubic and monocline phases could not be discriminated based on the 30.5°/21.3° intensity ratio, as they feature similar values in the integrated GIWAXS profiles.

A complete phase transformation of the as prepared nanostructures to orthorhombic is demonstrated upon ageing experiments. A 30.5°/15.1° intensity ratio of nearly 1.9 (Fig. 6(d) solid line) and a 30.5°/21.3° intensity ratio of nearly 0.6 (Fig. 6(d) circle symbols) resulted for the aged sample, better matching the expected values for the orthorhombic phase (1.8 and 0.8, respectively), and proving to be consistent to each other. The 30.5° and 15.1° peaks clearly split resulting in a doublet, with a net increase in intensity of the peak at larger 2θ for each doublet, indicating a domain size increase and a morphological evolution towards a highly anisotropic shape in agreement with TEM characterization (Fig. 2(b)). The two peaks at 15.1° and 30.5° can be thus assigned to 002/110 and 004/220 reflections, and the 21.3° one to the 112/020/200 reflection, of the orthorhombic phase (ICDD #01-072-7929), respectively. Since the 110 (220) peak results sharper, while the 002 (004) appears as a low intense shoulder, the [110] can be assumed as the anisotropic growth direction.

3.4 Shape and phase ligand assisted transformation. Olam addition

The $\theta/2\theta$ XRD (Fig. 6(e), solid line) and GIWAXS integrated profile (Fig. 6(e), circle symbol) for Olam 75 sample are different from each other, thus suggesting that they account for different species. The $\theta/2\theta$ XRD pattern (Fig. 6(e) solid line) is quite similar to that of the aged sample, therefore accounting for residual $CsPbBr_3$ nanocubes. On the other hand, the GIWAXS characterization (Fig. 6(e) circle symbol, and Fig. 6(k) 2D map), reveals an overall peak broadening in the radial profile and disappearance of the 15.1° peak, which indicate a decrease of the nanostructure domain size and the loss of the pristine phase, respectively. Notably, the suppression of the peak at 15.1° is compatible with a transition to the tetragonal phase where, as previously discussed, the 15.1° and 30.5° peaks are no more different diffraction orders form the same lattice planes, but independent reflections: 100 and 002/200, respectively. Therefore, the damping of the *h*00 reflections can be ascribed to the decrease of the crystalline domain in the *a*,*b* plane ([*h*00] and [0*k*0] are equivalent directions for the *P*4*mm* space group). On the other hand, the 002 reflection (around 30.3°) still features a significant contribution. These findings are therefore compatible with a tetragonal nanostructure anisotropically elongated along the *c* axis, which is expected to be relative to the newly formed nanowires. Such low crystallinity structures are only detected thanks to the peerless surface sensitivity of the GIWAXS technique: The detail-rich 2D data collection readily proves the orientational randomicity of the nanowires, allows excluding possible preferred orientations affecting relative intensities, and supports the 002 reflection as the main contribution to the 30.3° peak (i.e. the tetragonal structure with the *c* axis oriented along the nanowire). In the Olam 150 sample, a transformation of $CsPbBr_3$ stoichiometry into Cs_4PbBr_6 phase, as reported in literature to be induced by alkyl amine addition to the as prepared nanocubes and as suggested in the previously reported morphological and spectroscopic characterization, is confirmed by the XRD ($\theta/2\theta$) pattern (Fig. 7(b)) of the, featuring sharp peaks superimposed on a background ascribed to Olam, that well agrees with Cs_4PbBr_6.

3.5 Shape and phase ligand assisted transformation. Olac addition

XRD ($\theta/2\theta$) patterns (Figs. 6(f) and 7(c)) demonstrate that, irrespectively from the amount of Olac added (Olac 75 and Olac 150 samples), NPLs have an orthorhombic phase. The sharp 15.1° and 30.5° reflections clearly split into two contributions, with an intensity ratio (2.2) closely matching the value expected for the 002(110)/004(220) orthorhombic reflections, thus confirming the increase of the crystalline domain size, i.e. the lateral size as evidenced in TEM analysis (Fig. 4). Such sharp peaks indicate the preferential edge-on orientation and the crystallographic directions of the growth plane of the NPLs, which can reach hundreds nm size, as shown in Figs. 4(a)–4(d). Accordingly, the diffraction peak at 21.3° (112/020/200) remains broad and almost quenched (Fig. 6(f), solid line), being related to a crystallographic direction oriented across the small NPLs thickness.

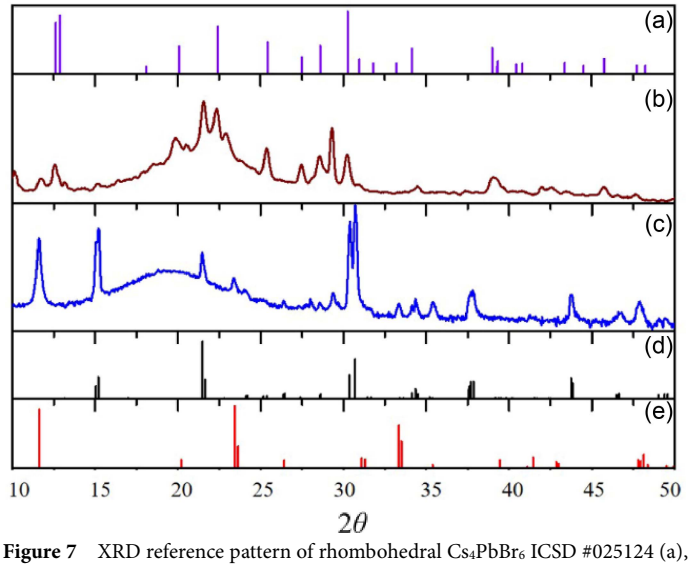

Figure 7 XRD reference pattern of rhombohedral Cs_4PbBr_6 ICSD #025124 (a), orthorhombic $CsPbBr_3$ ICDD #01-072-7929 (d) and Cs_3O ICSD # 015695 (e). XRD ($\theta/2\theta$) characterization of Olam 150 (b) and Olac 150 (c) samples.

4 Discussion

While the exceptional optoelectronic properties of colloidal $CsPbBr_3$ nanostructures have been already widely recognized, still their limited stability due to the ionic nature, the weak interaction of lead halide interlayers and the labile ligand/NC surface interaction [11, 48] remain critical issues for their application in devices. Here, the role of surface treatment/post synthetic procedures in the stability of the final $CsPbBr_3$ nanostructures is rationalized [14, 29–34, 39] and the mechanisms driving the size/shape transformation under different processing condition are depicted.

Focusing on the structure and surface chemistry of $CsPbBr_3$ NCs, it is generally accepted that the as prepared colloidal $CsPbBr_3$ nanocubes can be considered as an inorganic 3D network where the octahedral $[PbBr_6]^{4-}$ share each Br^- anion, at the corner, with the cesium occupying the cuboctahedral cavity and Olam and Olac adsorbed at the surface by hydrogen bonds (H••••Br) or coordinating (transition) metal, in equilibrium with free ligands in solution [11, 15].

The chemistry at the $CsPbBr_3$ NC surface recently emerged [11, 14, 48] crucial to understand the colloidal stability, optical and electronic properties and hence the technological potential of this class of material. The ^{1}H-NMR spectrum reported in Fig. 8(a) (black line) is in good agreement with previously reported results [48], and confirms that the oleylammonium bromide and oleate stabilizes the NC surface. It shows the typical broad resonances at 2.85 and 2.40 ppm ascribed to α-CH_2 of the oleylammonium and oleate, respectively, whose peak broadening and shift, with respect to corresponding resonances of the neat ligands, as reference (α-CH_2 of Olam and Olac, respectively [48], can be ascribed to the typical behaviour of tightly bound ligands [11] and ligand acid-base equilibrium [48]. At the same time, the peculiar resonance at δ = ~ 5.50 ppm can be ascribed to the alkene protons belonging to both ligands. Since the NCs have not been extensively purified, aiming at preserving their colloidal stability and structural integrity, the signals of the residual solvent (octadecene) and synthesis by-products (such as amide) are still clearly visible in the ^{1}H-NMR spectrum [48]. However, while the presence of negative (red) cross peaks in the NOESY spectrum (Fig. 8(b)) confirms that oleylammonium and oleate actually bind the NC surface and stabilize the $CsPbBr_3$ structure, octadecene and amide impurities are not interacting species with the NC surface. The surface chemistry of the NC can be, thus, shortly described NC(XX'), with X oleylammonium and X' bromide or oleate as X-type ligands [11].

Beside the surface chemistry, the accurate phase determination of all-inorganic nanosized colloidal $CsPbBr_3$ NCs is also critical due to several possible stoichiometry and crystal lattice distortions, thermodynamically favored at room temperature, of different crystalline phases featuring similar diffraction patterns [3, 16]. In addition, the nanosized regime, with its characteristic broadening of diffraction peaks, render phase discrimination even more difficult [3]. Though $CsPbBr_3$ NCs with a cubic perovskite structure are expected at high temperature, recent report [3] pointed out that the orthorhombic phase represents the thermodynamically stable structure at room temperature. However, the structural characterization here reported highlights that monocline or cubic phase, rather than orthorhombic XRD pattern, describes the structure of the as synthesized nanocubes. Prolonged moisture, light and air exposure finally induce morphological and structural change, with 8 nm-sized nanocubes transforming into the large (lateral size > 100 nm) anisotropic nanostructures having a clear orthorhombic phase, thus confirming the longer structural stability of this crystalline phase over cubic and monoclinic under ambient condition.

The morphological and spectroscopic investigation of the as prepared nanocubes upon different environmental condition described in the Results section evidence that post synthesis treatment such as dilution and addition of fresh (new) ligands are able to induce

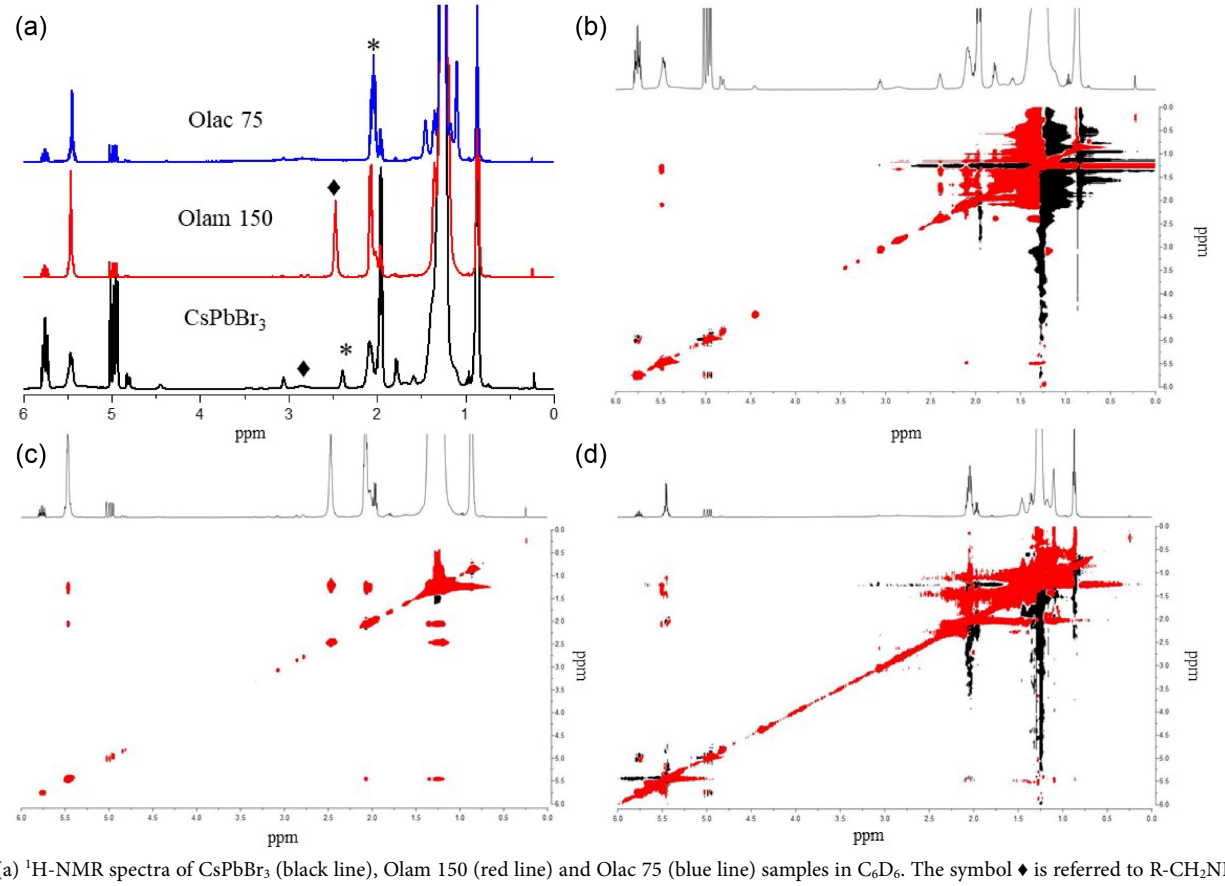

Figure 8 (a) ^{1}H-NMR spectra of $CsPbBr_3$ (black line), Olam 150 (red line) and Olac 75 (blue line) samples in C_6D_6. The symbol ♦ is referred to R-CH_2NH_2 of Olam ligand, the symbol ∗ to the R-CH_2COOH resonances of Olac ligand. NOESY spectra of $CsPbBr_3$ (b), Olam 150 (c) and Olac 75 (d) samples in C_6D_6.

morphological, spectroscopic and/or structural changes.

Interestingly upon dilution with an anhydrous organic solvent (hexane, toluene), the 8 nm sized $CsPbBr_3$ nanocubes evolve towards thinner 2D NPLs and smaller 3D nanostructures, thus corroborating the changes in the optical properties, including the PL blue shift, the multiple emission bands, and the increase in the FWHM. Changes of the emission band with respect to nanostructure concentration have been already reported by Di Stasio et al. [39], that found out concentration dependent PL emission band with a red shift of the emission at increasing concentration. Similarly, Tong et al. [43] described a PL emission blue shift of organic–inorganic perovskite NCs upon dilution, due to the formation of smaller nanostructures. These small nanostructures, rather than deriving from NC dissolution in the non-polar solvent (hexane), which is, in fact, a bad solvent for the NCs, can be reasonably thought to be originated by the solvent molecules penetration within the unprotected perovskite layers, due to the concomitant effect of partial desorption of the ligand and increased osmotic pressure, that breaks the as prepared NC into the smaller nanostructures. Nonetheless the TEM micrographs show along with small nanostructures very few large square shaped NPs, whose lateral size is greater than that of the starting nanocubes. Due to the low energy formation of $CsPbBr_3$ that does not require thermal activation to achieve high crystalline nanostructures, the concomitant surfactant-controlled co-precipitation of residual ions in solution, which proceeds with fast kinetics even at room temperature, cannot be ruled out and may result in the formation of bigger nanostructures, although at a very low extent [49].

Ligands desorption from the NC surface upon ambient, mainly moisture (and light), exposure during ageing of the as prepared nanocubes can be also potentially inferred to cause the averaged increase of the nanostructure size with the formation of bigger 3D and 2D anisotropic structures.

However, the post-synthesis addition of fresh ligands (Olam, OCTA, and Olac, NA see Scheme 1) has been found to have the strongest effect on the $CsPbBr_3$ shape (Figs. 3 and 4) and structural (Figs. 6 and 7) transformation ultimately resulting in the modification of photophysical properties (see Fig. 5 and Fig. S7 in the ESM).

The addition of alkyl amine has been widely reported to induce the transformation of the 3D $CsPbBr_3$ nanocubes into 0D Cs_4PbBr_6 [14, 29–34, 41], with each $[PbBr_6]^{4-}$ surrounded by 8 Cs^+ ions and the Br^- no longer shared between the $[PbBr_6]^{4-}$. The emission properties of Cs_4PbBr_6 NCs have been longer debated and are still unclear, as both intense emission properties and a complete quenching of the photoluminescence have been reported. Here, photo-inactive Cs_4PbBr_6 NCs form starting from nanocubes solution upon addition of high amount of Olam (> 0.15mmol/mL, Olam 150 sample) and similarly upon addition of OCTA (0.2 mmol/mL, Fig. S3(b) in the ESM). Addition of Olam (OCTA) at this concentration provokes an increase in the pH of the solution from 6 up to 8. The strong

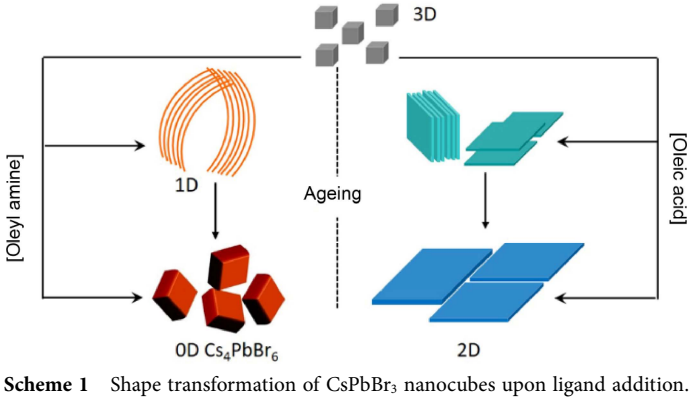

Scheme 1 Shape transformation of $CsPbBr_3$ nanocubes upon ligand addition. Scheme of the morphological transformation of the as prepared 3D $CsPbBr_3$ nanocubes to lower dimensional cesium lead halide derivatives.

binding affinity of Olam, in particular, and alkylamine, in general, for the Pb^{2+} ions can be considered the driving force that, through lead bromide depletion, causes distortion of the 3D $CsPbBr_3$, ending up into a completely different phase based on 0D Cs_4PbBr_6 [29].

However, here we are able to isolate an intermediate metastable 1D structures (Olam 75 sample) consisting of NWs, which, based on the structural characterization, are formed through a transition to $CsPbBr_3$ tetragonal phase. Compared to the 3D $CsPbBr_3$ nanocubes, the 1D NW structures formed upon addition of Olam at low concentration (0.075 mmol/mL) can be described as originated through a 3D distortion mechanism: Due to Olam-induced $PbBr_2$ depletion, the $[PbBr_6]^{4-}$ octahedra start to be disconnected and reordered into linear chains extended along the *c* axis of the tetragonal lattice. The NWs structures also originate by addition of neat OCTA at 0.08 M (Fig. S3(a) in the ESM). In both cases, the pH increases from pH = 6, of the as prepared nanocube colloidal solution to pH = 7 upon addition of 0.075 mmol/mL of Olam and 0.08 of OCTA. These 1D nanostructures very poorly emitting and unstable convert into a completely photo-inactive non perovskite structures after 1 week. Figure 8(a) (red line) reported the ^{1}H-NMR spectrum of the Olam added samples. It is worth noting that the Olam 50 sample rapidly transforms into the non-perovskite Cs_4PbBr_6 structure upon drying under vacuum required for NMR sample preparation. The ^{1}H-NMR spectrum is mainly dominated by the resonances of the neat oleyl amine, tightly bound at the NC surface, as also revealed by the NOESY spectrum (Fig. 8(c)). These results confirm that the oleylammonium bromide and oleylammonium oleate ion pair binding the as prepared $CsPbBr_3$ NC surface as X-type ligands have been completely removed upon addition of Olam. Indeed, under this condition the increase in the pH shifts the ligand acid-base equilibrium towards the base species (Olam and Oleate). However, the oleate moiety could not bind the surface of the NC, as X-type ligand as it requires an ion pair to preserve the NC stoichiometry and hence it is easily replaced by Olam, acting as an L-type ligand [11].

Conversely, the Olac addiction, that causes the pH decrease to pH = 4, will shift the acid-base equilibria of the ligands towards the protonated forms, that, as here reported, results in the transformation of nanocubes into NPLs [12–14]. The formation of NPLs during the synthesis has been already described in literature to be favored over nanocubes by the presence of alkyl carboxylic acid [14, 15, 17] or, similarly, by dropping inorganic bromidic acid [12, 21]. The acid-base equilibrium [14] between the organic (inorganic) acid and alkyl amine, which is an organic base, used as ligand in the reaction mixture, generates alkylammonium. The excess of alkyl ammonium has been demonstrated to compete with the Cs^+ ions at the surface [50] during the growing step and selectively slows down the growth along these directions, blocking specific surface sites, resulting in anisotropic NPLs.

Similarly, here, the pH decrease, upon post-synthesis addition of fresh Olac, effectively triggers the morphological evolution of the as prepared nanocubes into NPLs. The organic carboxylic acid shifts the Bronsted-Lowry equilibrium between the two Olam/Olac free ligands, promoting the protonation of Olam in solution with the formation of oleylammonium cation, $Olam^+$ and the protonation of the oleate. The ^{1}H NMR spectrum of the Olac 75 sample (Fig. 8(a), blue line) reveals that only the carboxylic acid binds the NC surface. We can reasonably assume that, upon addition of Olac, $Olam^+$ that binds more weakly the surface of $CsPbBr_3$ [21], can be completely removed by the freshly added Olac. $Olam^+$, dissolved in solution, may either replace the surface Cs^+ [21], thus partially changing the nanocrystals stoichiometry, which turns into in $Cs_{1-x}(Olam)_xPbBr_3$, or intercalate in the 3D nanostructure. Since $Olam^+$ (alkyl chain length nearly 2 nm) is larger than Cs^+ (ionic radius 167 pm) it cannot fit into the rigid 3D perovskite structures, therefore the

system splits into layers of lower dimensional network (2D) [51]. Although this substitution is thermodynamically not favoured, still the TEM micrographs of Olac 75 (Fig. 4 and similarly for sample treated with NA, see Fig. S4 in the ESM) provide a clear evidence of the formation of 2D nanostructures, 4 nm thick (nearly 3 multilayers), smaller than the as-prepared nanocubes (8 nm in later size). This morphological finding confirms the feasibility of fragmentation induced by *in situ* originated $Olam^+$ which is also corroborated by the spectroscopic characterization reported in Fig. 5 that shows blue shifted exciton absorption and PL feature, due to size dependence of the optical properties for quantum confined nanostructures. Meanwhile, the overall process results in a general increase in the NPLs lateral size that can even reach tens of nanometres. Indeed, the NOESY spectrum (Fig. 8(d)) of the Olac 75 exhibits negative cross peaks for Olac that results only loosely bound at the NC surface. On these bases, we can argue that the dynamic and labile interaction of Olac with the NC surface and the concomitant detachment of $Olam^+$ from the surface and its dissolution support the ligand-assisted aggregation process that results in the selective growth of 2D nanostructures with larger lateral size.

In order to get further insight in the mechanism behind the ligand assisted transformation, post synthetic treatments by using a mixture of NA, as alkyl carboxylic acid, and OCTA, as alkyl amine, at different molar ratios are carried out, to modulate the pH and the ligand acid-base equilibria. The alkyl base (B:, OCTA) and carboxylic acid (HA. NA) are expected to react with each other and generate BH^+A^- ($OCTA^+NA$) salt *in situ* and induce pH changes (Fig. S4 in the ESM), depending on their relative amount. When an equimolar (1:1) solution of OCTA:NA (0.1M:0.1M) is added to 1 mL of green colored colloidal solution of nanocubes for a post synthetic treatment, the solution turns into a white suspension in less than 15 minutes and the pH is found to increase at pH = 8. Such an evidence highlights that under this condition the obtained nanostructures are mainly based on larger Cs_4PbBr_6 rhombohedral nanostructures (Figs. S4(a) and S4(d) in the ESM). When OCTA:NA solution with molar ratio 0.6:1 (0.06M:0.1M) is used for post synthesis treatment, the pH of the colloidal solution becomes neutral and the TEM analysis of the sample clearly shows the formation of NW nanostructures (Fig. S4(b) in the ESM). Further reduction of OCTA (OCTA:NA 0.2:1, 0.02M:0.1M) shifts the pH to 4/5 and nanoplates structures (Figs. S4(c) and S4(e) in the ESM) can be easily recognized in the TEM micrograph, mainly assembled in face to face structures. Statistical analysis of the size (Fig. S4(e) in the ESM) reveals NPL having a thickness (4 nm σ% = 19%) smaller than the original nanocubes (8 nm) and a lateral size of 10 nm (σ% = 13%). The transformation of 3D nanocubes into 2D NPLs induced in this sample by OCTA:NA treatments corroborates the mechanism proposed for Olac 75 sample, relying on fragmentation/ligand assisted recrystallization that may occur due to the labile alkyl carboxylic acid binding of the NC surface and the concomitant dissolution of alkyl ammonium at more acidic pH.

The $\theta/2\theta$ XRD pattern reported in Fig. 6(f), related to the Olac 75 sample, closely matching that of the orthorhombic phase, highlights that the 002 and 110 (and similarly 004 and 220) represent the growing directions involved in the increased lateral size of the NPLs. Interestingly, the lateral size of the NPLs becomes even larger, with nanostructures preferring a face-on assembly on the TEM surface (Fig. 4(c)) either as the Olac concentration increases (Olac 150 sample), thus the pH decreases, or by ageing the Olac 75 samples. Therefore, fragmentation and reorganization/recrystallization into larger nanostructures can be kinetically controlled by pH and slowed down by decreasing the concentration of the added alkyl carboxylic acid. Such a mechanism that involves a pH decrease due to alkyl carboxylic acid addition and the formation of $Olam^+$ that controls the anisotropic growth, through Cs ions substitution and NC surface binding, is also demonstrated by structural characterization (Fig. 7(c)). The $\theta/2\theta$ XRD pattern of Olac 150 sample shows (Fig. 7(c)) a sharp reflection at 11.6° that can be ascribed to Cs_3O (Fig. 6(e) reference pattern), proving the Cs^+ release in solution. Since the Cs ions, responsible of the NPL lateral size growth, are not completely consumed in recrystallization process, the nanostructure becomes prone to air oxidation.

5 Conclusions

The study has established the key role played by ligands in the destabilization of $CsPbBr_3$ nanocubes upon post synthesis oleyl amine and oleic acid addition, dilution and ageing. The mechanism behind the observed transformations has been depicted thanks to a comprehensive morphological, spectroscopic and structural characterization. In particular the acid/base equilibrium between the two ligands acting as Lewis acid and base and/or the affinity of oleylammonium for lead halide have been demonstrated to promote the transformation of nanocubes into 2D NPLs or 1D NWs and 0D non perovskite rhombohedral nanostructures, upon oleic acid or oleyl ammine addition, respectively. Concomitantly, the dynamic between adsorbed and free ligands in solution and ligand solubility in non-polar solvent have been observed to induce fragmentation phenomena due to osmotic solvent swelling, resulting in the formation of smaller 3D and 2D nanostructures, upon dilution. Conversely, the low $CsPbBr_3$ energy formation, which makes the surfactant controlled recrystallization of free ions in solution a viable process at room temperature, results in an increase in the average size of the nanostructures. As a matter of fact, in order to protect $CsPbBr_3$ integrity and prevent structural, morphological and spectroscopic variations, all these equilibria need to be taken into account during processing of this material. This work demonstrates that a truly integrated investigation approach is able to provide original and unique findings essential for the fundamental understanding of the issues related to cesium lead halide perovskite stability, but also relevant for properly exploiting the potential of this type of material in technological applications

Acknowledgements

This work was financially supported by the MIUR PRIN 2015 (No. 2015XBZ5YA). The support of the Project of Industrial Research PON Best4y ARS01_00519 and the project FIRB Futuro in Ricerca (No. RBFR122HFZ) are recognized. The authors thank PON SISTEMA (No. PONa3_00369) for feasibility of using UV–Vis–NIR Spectrophotometer. Rocco Lassandro is acknowledged for his technical support in the X-Ray laboratory.

Electronic Supplementary Material: Supplementary material ( ) is available in the online version of this article at https://doi.org/10.1007/s12274-019-2371-2.

References

[1] Protesescu, L.; Yakunin, S.; Bodnarchuk, M. I.; Krieg, F.; Caputo, R.; Hendon, C. H.; Yang, R. X.; Walsh, A.; Kovalenko, M. V. Nanocrystals of cesium lead halide perovskites ($CsPbX_3$, X = Cl, Br, and I): Novel optoelectronic materials showing bright emission with wide color gamut. *Nano Lett.* **2015**, *15*, 3692–3696.

[2] Ha, S. T.; Su, R.; Xing, J.; Zhang, Q.; Xiong, Q. H. Metal halide perovskite nanomaterials: Synthesis and applications. *Chem. Sci.* **2017**, *8*, 2522–2536.

[3] Kovalenko, M. V.; Protesescu, L.; Bodnarchuk, M. I. Properties and potential optoelectronic applications of lead halide perovskite nanocrystals. *Science* **2017**, *358*, 745–750.

[4] Huang, H.; Bodnarchuk, M. I.; Kershaw, S. V.; Kovalenko, M. V.; Rogach, A. L. Lead halide perovskite nanocrystals in the research spotlight: Stability and defect tolerance. *ACS Energy Lett.* **2017**, *2*, 2071–2083.

[5] Liu, Q. H.; Wang, Y. H.; Sui, N.; Wang, Y. T.; Chi, X. C.; Wang, Q. Q.; Chen, Y.; Ji, W. Y.; Zou, L.; Zhang, H. Z. Exciton relaxation dynamics in photo-excited $CsPbI_3$ perovskite nanocrystals. *Sci. Rep.* **2016**, *6*, 29442.

[6] Liao, J. F.; Li, W. G.; Rao, H. S.; Chen, B. X.; Wang, X. D.; Chen, H. Y.; Kuang, D. B. Inorganic cesium lead halide $CsPbX_3$ nanowires for long-term stable solar cells. *Sci. China Mater.* **2017**, *60*, 285–294.

[7] Li, B.; Zhang, Y. N.; Fu, L.; Yu, T.; Zhou, S. J.; Zhang, L. Y.; Yin, L. W. Surface passivation engineering strategy to fully-inorganic cubic $CsPbI_3$ perovskites for high-performance solar cells. *Nat. Commun.* **2018**, *9*, 1076.

[8] Zhang, D. D.; Yu, Y.; Bekenstein, Y.; Wong, A. B.; Alivisatos, A. P.; Yang, P. D. Ultrathin colloidal cesium lead halide perovskite nanowires. *J. Am. Chem. Soc.* **2016**, *138*, 13155–13158.

[9] Kim, Y.; Yassitepe, E.; Voznyy, O.; Comin, R.; Walters, G.; Gong, X. W.; Kanjanaboos, P.; Nogueira, A. F.; Sargent, E. H. Efficient luminescence from perovskite quantum dot solids. *ACS Appl. Mater. Interfaces* **2015**, *7*, 25007–25013.

[10] Reichardt, C. *Solvents and Solvent Effects in Organic Chemistry*; 3rd ed. Wiley-VCH: Weinheim, Germany, 2003.

[11] De Roo, J.; Ibáñez, M.; Geiregat, P.; Nedelcu, G.; Walravens, W.; Maes, J.; Martins, J. C.; Van Driessche, I.; Kovalenko, M. V.; Hens, Z. Highly dynamic ligand binding and light absorption coefficient of cesium lead bromide perovskite nanocrystals. *ACS Nano* **2016**, *10*, 2071–2081.

[12] Udayabhaskararao, T.; Kazes, M.; Houben, L.; Lin, H.; Oron, D. Nucleation, growth, and structural transformations of perovskite nanocrystals. *Chem. Mater.* **2017**, *29*, 1302–1308.

[13] Cho, J.; Jin, H.; Sellers, D. G.; Watson, D. F.; Son, D. H.; Banerjee, S. Influence of ligand shell ordering on dimensional confinement of cesium lead bromide ($CsPbBr_3$) perovskite nanoplatelets. *J. Mater. Chem. C* **2017**, *5*, 8810–8818.

[14] Almeida, G.; Goldoni, L.; Akkerman, Q.; Dang, Z. Y.; Khan, A. H.; Marras, S.; Moreels, I.; Manna, L. Role of acid–base equilibria in the size, shape, and phase control of cesium lead bromide nanocrystals. *ACS Nano* **2018**, *12*, 1704–1711.

[15] Pan, A. Z.; He, B.; Fan, X. Y.; Liu, Z. K.; Urban, J. J.; Alivisatos, A. P.; He, L.; Liu, Y. Insight into the ligand-mediated synthesis of colloidal $CsPbBr_3$ perovskite nanocrystals: The role of organic acid, base, and cesium precursors. *ACS Nano* **2016**, *10*, 7943–7954.

[16] Liang, Z. Q.; Zhao, S. L.; Xu, Z.; Qiao, B.; Song, P. J.; Gao, D.; Xu, X. R. Shape-controlled synthesis of all-inorganic $CsPbBr_3$ perovskite nanocrystals with bright blue emission. *ACS Appl. Mater. Interfaces* **2016**, *8*, 28824–28830.

[17] Shamsi, J.; Dang, Z. Y.; Bianchini, P.; Canale, C.; Di Stasio, F.; Brescia, R.; Prato, M.; Manna, L. Colloidal synthesis of quantum confined single crystal $CsPbBr_3$ nanosheets with lateral size control up to the micrometer range. *J. Am. Chem. Soc.* **2016**, *138*, 7240–7243.

[18] Lignos, I.; Protesescu, L.; Emiroglu, D. B.; Maceiczyk, R.; Schneider, S.; Kovalenko, M. V.; deMello, A. J. Unveiling the shape evolution and halide-ion-segregation in blue-emitting formamidinium lead halide perovskite nanocrystals using an automated microfluidic platform. *Nano Lett.* **2018**, *18*, 1246–1252.

[19] Goodwin, C. A. P.; Reta, D.; Ortu, F.; Chilton, N. F.; Mills, D. P. Synthesis and electronic structures of heavy lanthanide metallocenium cations. *J. Am. Chem. Soc.* **2017**, *139*, 18714–18724.

[20] Zhang, D. D.; Eaton, S. W.; Yu, Y.; Dou, L. T.; Yang, P. D. Solution-phase synthesis of cesium lead halide perovskite nanowires. *J. Am. Chem. Soc.* **2015**, *137*, 9230–9233.

[21] Akkerman, Q. A.; Motti, S. G.; Srimath Kandada, A. R.; Mosconi, E.; D'Innocenzo, V.; Bertoni, G.; Marras, S.; Kamino, B. A.; Miranda, L.; De Angelis, F. et al. Solution synthesis approach to colloidal cesium lead halide perovskite nanoplatelets with monolayer-level thickness control. *J. Am. Chem. Soc.* **2016**, *138*, 1010–1016.

[22] Seth, S.; Samanta, A. A facile methodology for engineering the morphology of $CsPbX_3$ perovskite nanocrystals under ambient condition. *Sci. Rep.* **2016**, *6*, 37693.

[23] Sun, S. B.; Yuan, D.; Xu, Y.; Wang, A. F.; Deng, Z. T. Ligand-mediated synthesis of shape-controlled cesium lead halide perovskite nanocrystals via reprecipitation process at room temperature. *ACS Nano* **2016**, *10*, 3648–3657.

[24] Li, X. M.; Wu, Y.; Zhang, S. L.; Cai, B.; Gu, Y.; Song, J. Z.; Zeng, H. B. $CsPbX_3$ quantum dots for lighting and displays: Room-temperature synthesis, photoluminescence superiorities, underlying origins and white light-emitting diodes. *Adv. Funct. Mater.* **2016**, *26*, 2435–2445.

[25] Ramasamy, P.; Lim, D. H.; Kim, B.; Lee, S. H.; Lee, M. S.; Lee, J. S. All-inorganic cesium lead halide perovskite nanocrystals for photodetector applications. *Chem. Commun.* **2016**, *52*, 2067–2070.

[26] Doane, T. L.; Ryan, K. L.; Pathade, L.; Cruz, K. J.; Zang, H. D.; Cotlet, M.; Maye, M. M. Using perovskite nanoparticles as halide reservoirs in catalysis and as spectrochemical probes of ions in solution. *ACS Nano* **2016**, *10*, 5864–5872.

[27] Krieg, F.; Ochsenbein, S. T.; Yakunin, S.; Ten Brinck, S.; Aellen, P.; Süess, A.; Clerc, B.; Guggisberg, D.; Nazarenko, O.; Shynkarenko, Y. et al. Colloidal $CsPbX_3$ (X = Cl, Br, I) nanocrystals 2.0: Zwitterionic capping ligands for improved durability and stability. *ACS Energy Lett.* **2018**, *3*, 641–646.

[28] Swarnkar, A.; Marshall, A. R.; Sanehira, E. M.; Chernomordik, B. D.; Moore, D. T.; Christians, J. A.; Chakrabarti, T.; Luther, J. M. Quantum dot–induced phase stabilization of α-$CsPbI_3$ perovskite for high-efficiency photovoltaics. *Science* **2016**, *354*, 92–95.

[29] Akkerman, Q. A.; Abdelhady, A. L.; Manna, L. Zero-dimensional cesium lead halides: History, properties, and challenges. *J. Phys. Chem. Lett.* **2018**, *9*, 2326–2337.

[30] Palazon, F.; Almeida, G.; Akkerman, Q. A.; De Trizio, L.; Dang, Z. Y.; Prato, M.; Manna, L. Changing the dimensionality of cesium lead bromide nanocrystals by reversible postsynthesis transformations with amines. *Chem. Mater.* **2017**, *29*, 4167–4171.

[31] Akkerman, Q. A.; Park, S.; Radicchi, E.; Nunzi, F.; Mosconi, E.; De Angelis, F.; Brescia, R.; Rastogi, P.; Prato, M.; Manna, L. Nearly monodisperse insulator Cs_4PbX_6 (X = Cl, Br, I) nanocrystals, their mixed halide compositions, and their transformation into $CsPbX_3$ nanocrystals. *Nano Lett.* **2017**, *17*, 1924–1930.

[32] Liu, Z. K.; Bekenstein, Y.; Ye, X. C.; Nguyen, S. C.; Swabeck, J.; Zhang, D. D.; Lee, S. T.; Yang, P. D.; Ma, W. L.; Alivisatos, A. P. Ligand mediated transformation of cesium lead bromide perovskite nanocrystals to lead depleted Cs_4PbBr_6 nanocrystals. *J. Am. Chem. Soc.* **2017**, *139*, 5309–5312.

[33] Udayabhaskararao, T.; Houben, L.; Cohen, H.; Menahem, M.; Pinkas, I.; Avram, L.; Wolf, T.; Teitelboim, A.; Leskes, M.; Yaffe, O. et al. A mechanistic study of phase transformation in perovskite nanocrystals driven by ligand passivation. *Chem. Mater.* **2018**, *30*, 84–93.

[34] De Weerd, C.; Lin, J. B.; Gomez, L.; Fujiwara, Y.; Suenaga, K.; Gregorkiewicz, T. Hybridization of single nanocrystals of Cs_4PbBr_6 and $CsPbBr_3$. *J. Phys. Chem. C* **2017**, *121*, 19490–19496.

[35] Zhu, H. M.; Trinh, M. T; Wang, J.; Fu, Y. P.; Joshi, P. P.; Miyata, K.; Jin, S.; Zhu, X. Y. Organic cations might not be essential to the remarkable properties of band edge carriers in lead halide perovskites. *Adv. Mater.* **2017**, *29*, 1603072.

[36] Eperon, G. E.; Ginger, D. S. B-Site metal cation exchange in halide perovskites. *ACS Energy Lett.* **2017**, *2*, 1190–1196.

[37] Maes, J.; Balcaen, L.; Drijvers, E.; Zhao, Q.; De Roo, J.; Vantomme, A.; Vanhaecke, F.; Geiregat, P.; Hens, Z. Light absorption coefficient of $CsPbBr_3$ perovskite nanocrystals. *J. Phys. Chem. Lett.* **2018**, *9*, 3093–3097.

[38] Bekenstein, Y.; Koscher, B. A.; Eaton, S. W.; Yang, P. D.; Alivisatos, A. P. Highly luminescent colloidal nanoplates of perovskite cesium lead halide and their oriented assemblies. *J. Am. Chem. Soc.* **2015**, *137*, 16008–16011.

[39] Di Stasio, F.; Imran, M.; Akkerman, Q. A.; Prato, M.; Manna, L.; Krahne, R. Reversible concentration-dependent photoluminescence quenching and change of emission color in $CsPbBr_3$ nanowires and nanoplatelets. *J. Phys. Chem. Lett.* **2017**, *8*, 2725–2729.

[40] Lv, L. F.; Xu, Y. B.; Fang, H. H.; Luo, W. J.; Xu, F. J.; Liu, L. M.; Wang, B. W.; Zhang, X. F.; Yang, D.; Hu, W. D. et al. Generalized colloidal synthesis of high-quality, two-dimensional cesium lead halide perovskite nanosheets and their applications in photodetectors. *Nanoscale* **2016**, *8*, 13589–13596.

[41] Palazon, F.; Urso, C.; De Trizio, L.; Akkerman, Q.; Marras, S.; Locardi, F.; Nelli, I.; Ferretti, M.; Prato, M.; Manna, L. Postsynthesis transformation of insulating Cs_4PbBr_6 nanocrystals into bright perovskite $CsPbBr_3$ through physical and chemical extraction of CsBr. *ACS Energy Lett.* **2017**, *2*, 2445–2448.

[42] Imran, M.; Di Stasio, F.; Dang, Z. Y.; Canale, C.; Khan, A. H.; Shamsi, J.; Brescia, R.; Prato, M.; Manna, L. Colloidal synthesis of strongly fluorescent $CsPbBr_3$ nanowires with width tunable down to the quantum confinement regime. *Chem*. *Mater*. **2016**, *28*, 6450–6454.

[43] Tong, Y.; Ehrat, F.; Vanderlinden, W.; Cardenas-Daw, C.; Stolarczyk, J. K.; Polavarapu, L.; Urban, A. S. Dilution-induced formation of hybrid perovskite nanoplatelets. *ACS Nano* **2016**, *10*, 10936–10944.

[44] Sichert, J. A.; Tong, Y.; Mutz, N.; Vollmer, M.; Fischer, S.; Milowska, K. Z.; García Cortadella, R.; Nickel, B.; Cardenas-Daw, C.; Stolarczyk, J. K. et al. Quantum size effect in organometal halide perovskite nanoplatelets. *Nano Lett*. **2015**, *15*, 6521–6527.

[45] Ravi, V. K.; Swarnkar, A.; Chakraborty, R.; Nag, A. Excellent green but less impressive blue luminescence from $CsPbBr_3$ perovskite nanocubes and nanoplatelets. *Nanotechnology* **2016**, *27*, 325708.

[46] De Weerd, C.; Gomez, L.; Zhang, H.; Buma, W. J.; Nedelcu, G.; Kovalenko, M. V.; Gregorkiewicz, T. Energy transfer between inorganic perovskite nanocrystals. *J*. *Phys*. *Chem*. *C* **2016**, *120*, 13310–13315.

[47] Cottingham, P.; Brutchey, R. L. On the crystal structure of colloidally prepared $CsPbBr_3$ quantum dots. *Chem*. *Commun*. **2016**, *52*, 5246–5249.

[48] Grisorio, R.; Di Clemente, M. E.; Fanizza, E.; Allegretta, I.; Altamura, D.; Striccoli, M.; Terzano, R.; Giannini, C.; Irimia-Vladu, M.; Suranna, G. P. Exploring the surface chemistry of cesium lead halide perovskite nanocrystals. *Nanoscale* **2019**, *11*, 986–999.

[49] Protesescu, L.; Yakunin, S.; Nazarenko, O.; Dirin, D. N.; Kovalenko, M. V. Low-cost synthesis of highly luminescent colloidal lead halide perovskite nanocrystals by wet ball milling. *ACS Appl*. *Nano Mater*. **2018**, *1*, 1300–1308.

[50] Ravi, V. K.; Santra, P. K.; Joshi, N.; Chugh, J.; Singh, S. K.; Rensmo, H.; Ghosh, P.; Nag, A. Origin of the substitution mechanism for the binding of organic ligands on the surface of $CsPbBr_3$ perovskite nanocubes. *J*. *Phys*. *Chem*. *Lett*. **2017**, *8*, 4988–4994.

[51] Boix, P. P.; Agarwala, S.; Koh, T. M.; Mathews, N.; Mhaisalkar, S. G. Perovskite solar cells: Beyond methylammonium lead iodide. *J*. *Phys*. *Chem*. *Lett*. **2015**, *6*, 898–907.

Table of contents

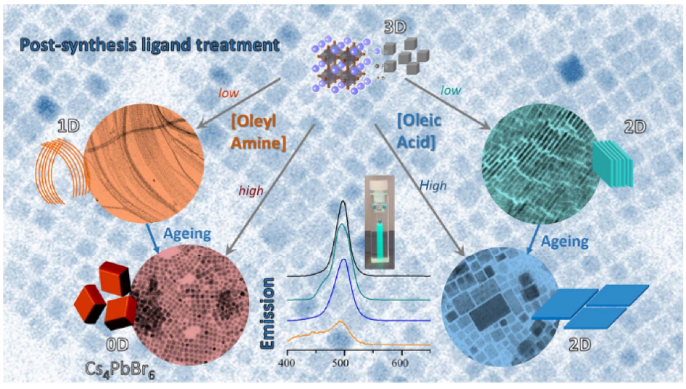

Ligand induced shape and phase evolution of three-dimensional (3D) $CsPbBr_3$ nanocubes into two-dimensional (2D) nanoplates, one-dimensional (1D) nanowires, and zero-dimensional (0D) nanostructures.

Electronic Supplementary Material

Post-synthesis phase and shape evolution of $CsPbBr_3$ colloidal nanocrystals: The role of ligands

Elisabetta Fanizza[1,2,§] (✉), Francesca Cascella[1,†,§], Davide Altamura[3], Cinzia Giannini[3], Annamaria Panniello[2], Leonardo Triggiani[1,2], Francesca Panzarea[1], Nicoletta Depalo[2], Roberto Grisorio[4,5], Gianpaolo Suranna[4,5], Angela Agostiano[1,2], M. Lucia Curri[1,2], and Marinella Striccoli[2] (✉)

[1] *Dipartimento di Chimica, Università degli Studi di Bari "A. Moro", Via Orabona 4 , 70126 Bari, Italy*
[2] *CNR-Istituto per i Processi Chimico Fisici, S. S. Bari, Via Orabona, 4, 70126 Bari, Italy*
[3] *CNR-Istituto di Cristallografia, Via Amendola, 122/O, 70126 Bari, Italy*
[4] *Dipartimento di Ingegneria Civile, Ambientale, del Territorio, Edile e di Chimica (DICATECh), Politecnico di Bari, Via Orabona 4, 70125, Italy*
[5] *CNR-NANOTEC- Istituto di Nanotecnologia, Via Monteroni 73100 Lecce, Italy*
[†] *Present Address: Max Planck Institute for Dynamics of Complex Technical Systems, Physical and Chemical Foundations of Process Engineering, Sandtorstr.1, D-39106 Magdeburg, Germany*
[§] *Elisabetta Fanizza and Francesca Cascella contributed equally to this work.*

Supporting information to https://doi.org/10.1007/s12274-019-2371-2

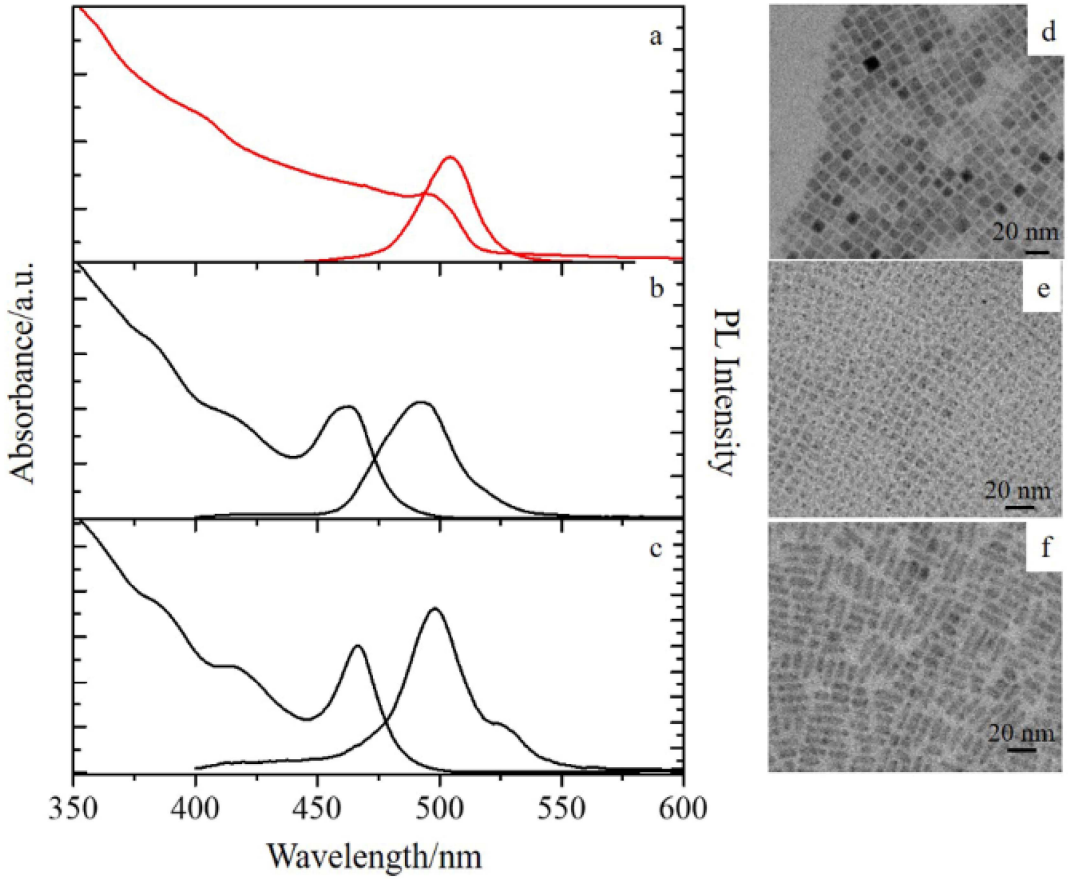

Figure S1 UV-Vis absorbance and PL spectra (a-b) and TEM micrographs (d-e) of the as prepared CsPbBr3 nanocubes collected as pellet after centrifugation of the reaction mixture (a,d), whose size is nearly 8 nn, and of nanostructures collected in the supernatant (b, e), having a size of nearly 4 nm. Spectroscopic (c) and morphological (f) characterization of the supernatant fraction reported in (b, e) after addition of 0.075 mmol/mL of Olac.

Address correspondence to Elisabetta Fanizza, elisabetta.fanizza@uniba.it; Marinella Striccoli, m.striccoli@ba.ipcf.cnr.it

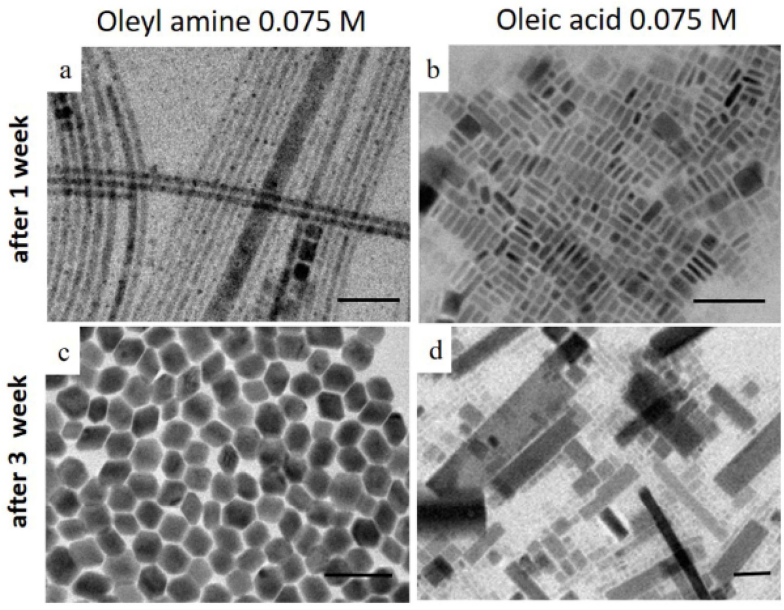

Figure S2 TEM micrographs of oleyl amine treated (a,c) and oleic acid treated (b, d) CsPbBr3 nanocubes, after 1 week (a,b) and after three weeks (c,d). Ligand concentration 0.075mmol/ml (0.075M). Scale bar 50 nm.

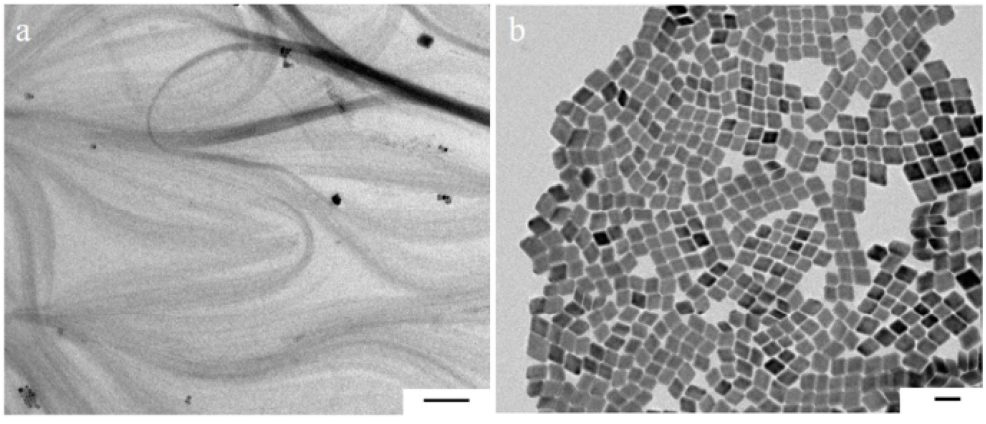

Figure S3 TEM micrographs of $CsPbBr_3$ nanocube sample after treatment with octylamine 0.08M (a) and 0.2M (b). Scale bar 50 nm.

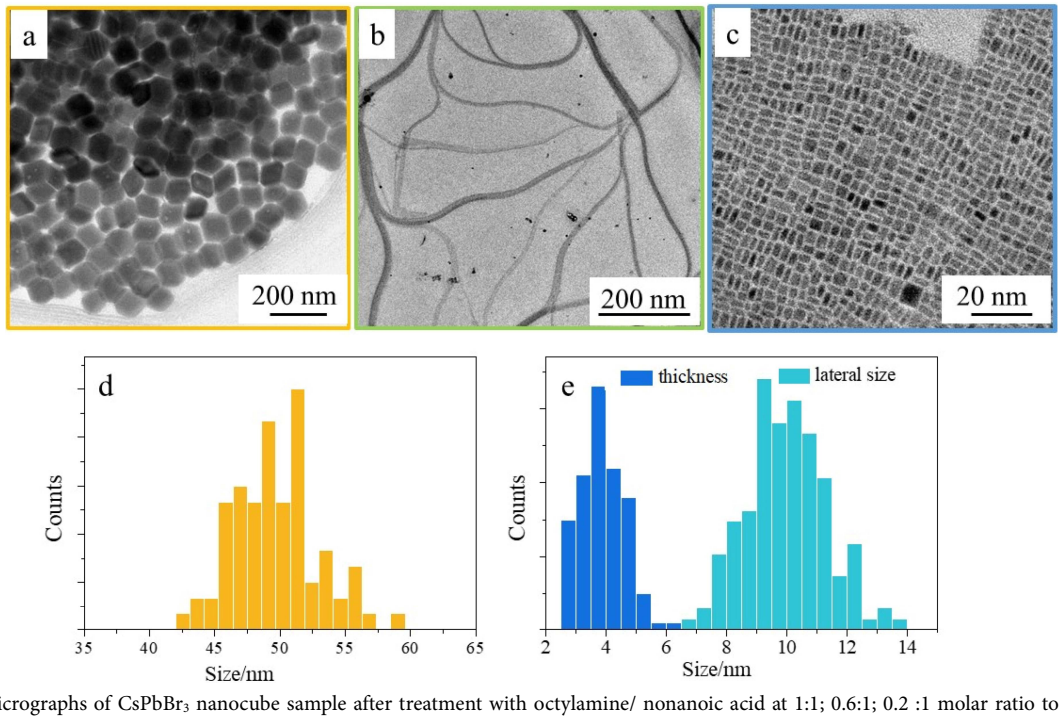

Figure S4 TEM micrographs of $CsPbBr_3$ nanocube sample after treatment with octylamine/ nonanoic acid at 1:1; 0.6:1; 0.2 :1 molar ratio to 1 mL of as prepared $CsPbBr_3$ colloidal solution.

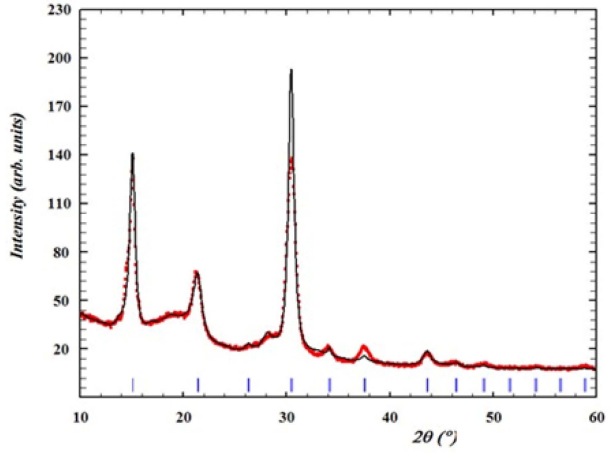

Figure S5 Experimental (red line, as in Figure 4e before background interpolation) and calculated (black line) XRD patterns of the as prepared $CsPbBr_3$ nanocubes .

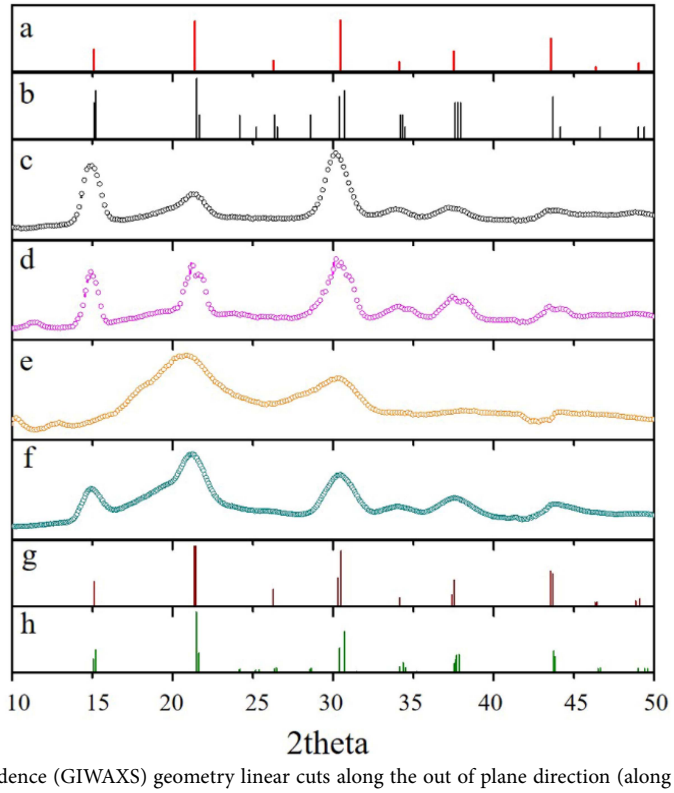

Figure S6 XRD patterns in grazing incidence (GIWAXS) geometry linear cuts along the out of plane direction (along the white arrows in the 2D maps in Figure 4l-o) of the as prepared (c), aged (d), 0.075 mmol/mL Olam treated (e) and 0.075 mmol/mL Olac treated (f) CsPbBr3 NCs. Reference XRD patterns for (a) cubic (ICSD # 01-072-7930), (b) monoclinic (ICDD #18-0364), (g) tetragonal (ICSD #01-074-6645) and (h) orthorhombic (ICSD #01-072-7929).

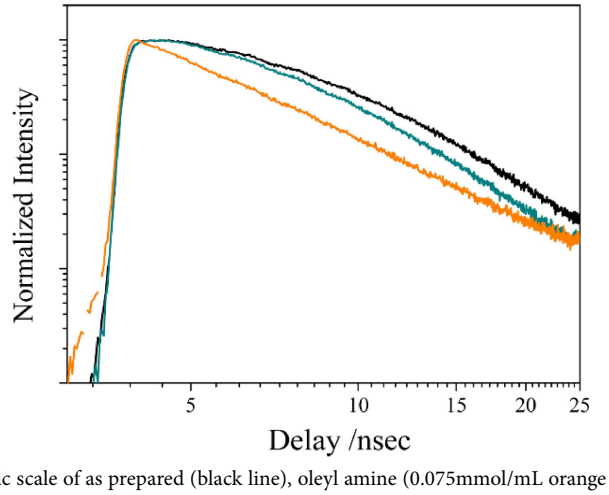

Figure S7 TCSPC decay on double logarithmic scale of as prepared (black line), oleyl amine (0.075mmol/mL orange line) and oleic acid (0.075mmol/mL cyan line) treated samples.

Table S1 Average lifetimes calculated by fitting the PL decay with a tri-exponential function where A, B1, B2, and B3 are constants, t is time, and τ1, τ2, and τ3 represent the decay lifetimes corresponding to the intrinsic exciton relaxation, the interaction between excitons and phonons, and the interaction between excitons and defects, respectively.

	τ1 (nsec)	B1 %	τ2 (nsec)	B2 %	τ3 (nsec)	B3 %	τav (nsec)
As synthesized	0.87±0.07	-3.71	4.1± 0.01	83.13	14.6±0.2	20.58	6.4 ± 0.04
0.075M Olac processing	0.3 ±0.01	-1.95	3.7± 0.01	87.79	14.2±0.1	14.16	5.3 ± 0.02
0.075M Olam processing	0.98±0.01	14.65	3.2± 0.04	61.73	14.1 ±0.3	23.62	5.5 ± 0.07

$$A(t) = A + B_1 \exp\left(-\frac{t}{\tau_1}\right) + B_2 \exp\left(-\frac{t}{\tau_2}\right) + B_3 \exp\left(-\frac{t}{\tau_3}\right).$$

The average lifetime (τ_{av}) has been calculated by:

$$\tau_{av} = \frac{B_1\tau_1^2 + B_2\tau_2^2 + B_3\tau_3^2}{B_1\tau_1 + B_2\tau_2 + B_3\tau_3}$$

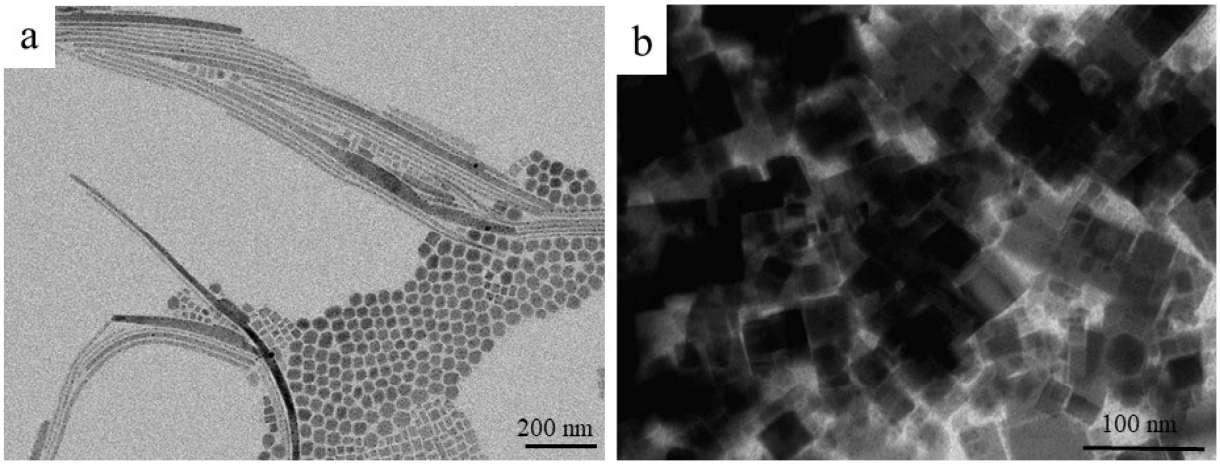

Figure S8 TEM micrographs of the precipitates of Olam 75 and Olac 75 treated $CsPbBr_3$ samples dispersed in anhydrous hexane.